energy&fuels

pubs.acs.org/EF

Article

Selective Hydroconversion of Polyaromatics into High-Density Endothermic Aviation Fuel over Highly Dispersed Pt/FAU Catalyst

Xiaopo Niu, Feipeng Huang, Wenli Zhao, Danni Liu, Yue Qin, Xiangwen Zhang, Hanfeng Lu, Quanli Ke, and Qingfa Wang*

Cite This: *Energy Fuels* 2025, 39, 12551−12568

Read Online

ACCESS | Metrics & More | Article Recommendations | Supporting Information

ABSTRACT: Selective hydroconversion of polyaromatics enriched in biomass pyrolysis oil into alkyladamantanes (PSA) and multibranched polycycloalkanes (SRO) for high-density endothermic aviation fuels (HEAFs) is a pivotal technological approach to satisfying the growing energy demand of the aerospace sector and mitigating the enormous pressure of environmental pollution. Herein, zeolites with MFI, FER, *BEA, and FAU topologies supported Pt catalysts, fabricated via an enhanced strong electrostatic adsorption strategy, were used to investigate the conversion route of phenanthrene in a fixed-bed reactor, and the products were identified using a comprehensive GC×GC-MS/FID device. Highly dispersed Pt clusters on the as-synthesized bifunctional catalysts were confirmed by XRD and HRTEM techniques. Compared to Pt/FER catalyst, Pt/MFI exhibited an ascendant deep hydrosaturation ability with perhydrophenanthrene as the main product at 180−280 °C. In contrast, significantly higher amounts of PSA and SRO were yielded on Pt/BEA and Pt/FAU owing to the favorable match between the dimensions of these species and the porous channels. The conversion pathway was established as follows: phenanthrene preferentially undergoes hydrosaturation, followed by skeletal rearrangement and cycloisomerization to generate PSA and SRO, ultimately resulting in the formation of cracking products. Monte Carlo simulations further verified that PSA and SRO primarily form within the pores and supercages of acid zeolites. Notably, Pt/FAU catalyst exhibited a significantly high HEAFs yield of 42.6 wt %. The prepared HEAFs demonstrated a density of 0.957 g/mL, net heat of combustion of 40.3 MJ/L, and ignition delay time of 2935 ms. These properties surpass those of JP-10, underscoring their exceptional potential in advanced aerospace applications.

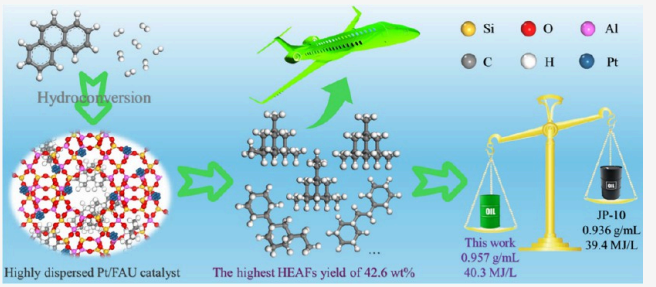

1. INTRODUCTION

Liquid hydrocarbon fuels serve as the primary power source for aerospace vehicles, missiles, and various weapon systems, significantly affecting aircraft performance, including flight speed, cruising range, and payload capacity.[1−3] Elevating the density of fuel within a settled tank can improve the energy furnished per unit volume, availably enhancing propulsion properties.[4] Attentively, an extra crucial role of aviation fuels is to cool structural components that become dynamically heated owing to friction during supersonic flight, necessitating fuels with splendid endothermic capabilities.[5,6] As the demand for high-density endothermic aviation fuels (HEAFs) continues to rise alongside advancements in hypersonic technology, there is an impatient need to exploit effective solutions.[1] Traditionally, HEAFs like JP-10 are produced through polymerization, hydrogenation, and rearrangement of the cyclopentadiene fraction obtained from petroleum refining. However, the yield of cyclopentadiene is low, only 14 kg/ton from naphtha cracking and 10−20 g/ton from coal tar extraction, making it hard to meet the desires of aerospace evolution.[3] Furthermore, in light of the strategic goals of carbon peak and carbon neutrality, environmental regulations are becoming increasingly stringent, prompting the aviation sector to reduce emissions.[7,8] It is imperative to explore novel and efficient synthetic routes to heighten HEAFs production, while slashing the discharge of hazardous substances.

Polycyclic aromatics (PAHs) such as naphthalene, fluorene, and phenanthrene are lavish in biomass pyrolysis oil and tar, but their effective processing remains a challenge for refineries due to their low reactivity, stemming from enormous resonance energy and steric hindrance.[9−12] Often incinerated for electricity generation, PAHs represent a prominent waste of resources and contribute to harmful emissions. However, the high energy density of these PAHs and coincident carbon numbers (C_9−C_{15}) with aviation fuels make them promising

Received: May 4, 2025
Revised: June 9, 2025
Accepted: June 12, 2025
Published: June 19, 2025

https://doi.org/10.1021/acs.energyfuels.5c02305
Energy Fuels 2025, 39, 12551−12568

candidates for the synthesis of HEAFs components, particularly alkyladamantanes (PSA) and multibranched polycycloalkanes (SRO), which exhibit high energy density, large volumetric net heat of combustion, remarkable endothermic performance, and outstanding thermal oxidation stability.[13−16] Transforming inert PAHs into PSA and SRO species not only enables the high-value utilization of pyrolysis oil but also provides an effective route for HEAFs production, while mitigating environmental pollution concerns. Typically, complicated processes such as hydrosaturation, rearrangement, isomerization, and ring opening are involved in the transformation of PAHs into HEAFs, resulting in interior yield of PSA and SRO compounds.[14] While enormous works have focused on deep hydrosaturation and (hydro)cracking of PAHs to manufacture saturated cycloparaffins and monocyclic aromatics, systematic researches on the selective hydroconversion of PAHs to HEAFs are limited.[17−19] Sulfide,[20−22] noble metal,[17,23−25] phosphide,[12,26] and carbide catalysts[27,28] have been extensively investigated for hydrosaturation reactions, while acidic zeolite catalysts like HY, Hβ, and USY[29−31] have been adopted for the (hydro)cracking of PAHs. Notably, bifunctional catalysts comprising active metals and acid zeolites illustrate exceptional catalytic properties in the selective hydroconversion of PAHs, wherein metal sites are responsible for the hydrosaturation of an aromatic ring, while acidic sites dominate isomerization and ring opening of polycyoalkanes.[14]

Recently, Brito et al.[32] examined the hydroconversion of perhydrophenanthrene (PHP) using a dual-bed catalyst at 280 °C and 60 bar. In the process, phenanthrene (PHE) was first hydrosaturated over Pt/Al_2O_3 to produce PHP, which was then converted into PSA and cracking products on the Pt/H-USY catalyst, demonstrating the feasibility for hydrogenating PAHs to HEAFs components. However, the yields of PSA and SRO were relatively low, at only 6% and 8%, respectively. Subsequently, Brito et al.[33] explored the conversion of PHP over Pt/Beta and Pt/ASA catalysts, assessing the influence of the support's porous structure on product selectivity and achieving a modest increase in PSA yield. Nonetheless, the reaction networks proposed by Brito et al.[32,33] are quite complicated, and the yield of HEAFs remains suboptimal. In contrast, one-step hydroconversion of PAHs yielding high quantities of HEAFs is more desirable. Wang et al.[34] investigated the ring-shift hydroisomerization of fluorene on zeolites and SiO_2−Al_2O_3-supported Pt catalysts, proposing a conversion pathway. The supreme yield of 9% for PSA, primarily consisting of 1-propyladamantane, was acquired over the Pt/MY catalyst. It is evident that the current literature chiefly focuses on the transformation of PAHs into PSA, with restricted attention on the formation of SRO. Typically, PSA shows higher energy density and thermal oxidation stability, while SRO offers strengthened endothermic capacities and generates less carbon deposition during combustion, making them indispensable components in HEAFs.[2] Importantly, the formation mechanisms of PSA and SRO via the hydroconversion of PAHs on bifunctional metal/zeolite catalysts remain unclear and lack systematic investigation.

The texture properties of bifunctional metal/zeolite catalysts are pivotal for reinforcing the HEAFs yield during the hydroconversion of PAHs. To consolidate the yield of PSA, Li et al.[35] regulated the mesopore structure and acid distribution of Pt/USY catalyst through NaOH-induced etching resulting in a reduced B_S/B_T ratio that inhibited cracking reactions and increased PSA yield to 32%. Similarly, Wang et al.[36] utilized oxalic acid to adjust the acidity of Pt/USY, demonstrating that acid treatment could enhance the yield of isomerization products from PHE. Furthermore, Zhao et al.[13] described the hydroisomerization network of acenaphthene on USY-supported Pt catalysts with varying degrees of demetallization, illustrating that larger pore sizes facilitated the diffusion of intermediates, thereby improving PSA yield. In addition to the zeolite support, the properties of the active metal also obviously affect catalytic performance. The wet impregnation method is a commonly employed technique for the preparation of supported catalysts, but it often results in a broad distribution of metal particle sizes and weak metal−support interactions, which can hinder the effective dispersion of active metals.[37] Enhanced strong electrostatic adsorption tactics can improve the dispersion of active metal and boost the metal−support interactions, as validated in our previous reports.[17,38] Highly dispersed active metals can interact more effectively with the acidic sites in zeolites, forming electron-deficient metal species. This is beneficial for strengthening the chemical adsorption of PAHs, thus promoting the selective hydroconversion performances.

In this work, to elucidate the mechanism of selective hydroconversion of PAHs and intensify the yields of PSA and SRO components in HEAHs, acid zeolites with disparate topological structures, including MFI, FER, *BEA, and FAU (Figure 1), were employed to prepare highly dispersed Pt

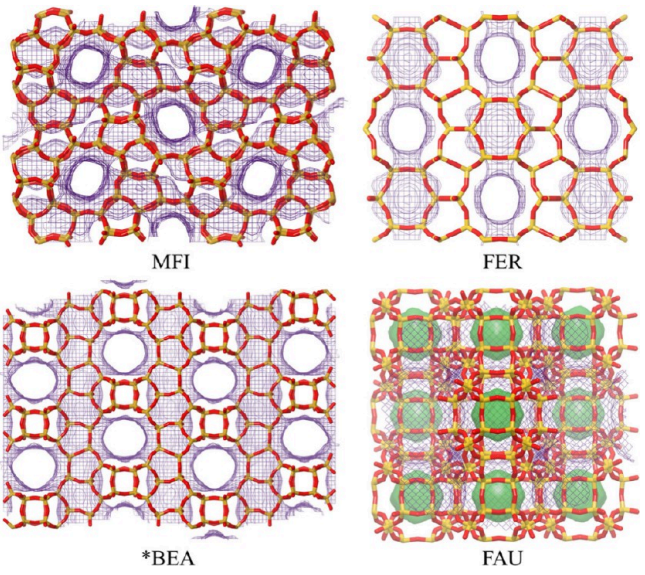

Figure 1. Schematic illustration of the topological skeleton and porous structure of MFI, FER, *BEA, and FAU zeolites (indigo mesh: channel systems; cyan: cages).

catalysts using an enhanced strong electrostatic adsorption strategy. Hydroconversion of phenanthrene, a representative species of PAHs, was conducted in a down-flow stainless fixed-bed microreactor at 180−280 °C under 40 bar. A comprehensive two-dimensional gas chromatography−mass spectrometry (GC × GC-MS/FID) device was employed to accurately identify the liquid products. The conversion network of phenanthrene was successfully established. Notably, Pt/FAU catalyst showed the maximal yield of HEAFs at 42.6%, which is the optimal performance reported in literature to our

https://doi.org/10.1021/acs.energyfuels.5c02305
Energy Fuels 2025, 39, 12551−12568

knowledge. Additionally, the formation mechanisms of PSA and SRO components were further verified through Monte Carlo simulations. This work furnishes a vital theoretical foundation for developing innovative manufacturing approaches for HEAFs based on the hydroconversion of PAHs.

2. EXPERIMENTAL SECTION

2.1. Materials. Tetraammineplatinum nitrate ($(NH_3)_4Pt(NO_3)_2$, Pt ≥ 50%) was purchased from Macklin, China. Phenanthrene (PHE, 97% purity) was obtained from TCI, Japan. *n*-Octane (99% purity) was supplied by Meryer, China. Acidic zeolites including ZSM-5, ZSM-35, *β*, and Y were provided by Nanjing Jicang Nano Technology Co., Ltd. Milli-Q water (18.2 MΩ·cm) was used in the experiments.

2.2. Synthesis of Highly Dispersed Bifunctional Pt/Zeolite Catalysts. Typically, a series of highly dispersed Pt/zeolite catalysts supported on ZSM-5, ZSM-35, *β*, and Y zeolites with various topological structures were prepared using an enhanced strong electrostatic adsorption method.[39,40] The Pt loading in series catalysts was set to 1.80 wt %. Briefly, the required amount of metal precursor ($Pt(NH_3)_4(NO_3)_2$) was dispersed in H_2O with a volume equivalent to the saturated water absorption of zeolite. Meanwhile, the pH of the solution was regulated to 11.5 adopting NH_4OH. Subsequently, the as-prepared metal precursor solution and zeolite were mixed uniformly in a flask for the electrostatic adsorption process. After that, the resulting samples were dried at 80 °C overnight under vacuum and roasted at 450 °C for 4 h (1 °C/min). The obtained samples were denoted as Pt/MFI, Pt/FER, Pt/BEA, and Pt/FAU, respectively. Finally, the gained catalysts were extruded into 380−550 *μ*m particles for subsequent catalytic activity evaluations.

2.3. Catalyst Characterization. Powder X-ray diffraction (XRD) patterns were employed to determine the skeleton structure and crystallinity of a series of Pt catalysts, which were performed on a Rigaku smartlab diffractometer (40 kV, 150 mA) in the 2*θ* range of 5−90° with a scanning rate of 5°/min using a Ni-filtered Cu K*α* (*λ* = 1.5406 Å) radiation source. The morphology and Pt metal dispersion were examined by using a JEOL JEM-F200 field emission transmission electron microscope (FETEM) outfitted with an energy dispersive spectrometer (EDS) at an accelerating voltage of 200 kV. A Quantachrome Autosorb-iQ2-MP equipment was used to analyze the nitrogen adsorption−desorption isotherms of the prepared catalysts at −196 °C. Before the measurements, 0.20 g of sample was deaerated at 300 °C and 10 mbar for 12 h. The total specific surface area (S_{BET}) was calculated by employing the Brunauer−Emmett−Teller (BET) formula, while the micropore surface area (S_{micro}) and volume (V_{micro}) were obtained through using the *t*-plot method. Besides, the adsorption data of nitrogen at P/P_0 = 0.99 was adopted to estimate the total pore volume (V_{total}). The practical metal loading and silica−alumina ratio in different Pt catalysts were ascertained via inductively coupled plasma optical emission spectrometry (ICP-OES) executed on Agilent 7700x equipment. Aqua regia and hydrofluoric acid were employed to dissolve the samples, and excess hydrofluoric acid was complexed with boric acid.

Temperature-programmed desorption of ammonia (NH_3-TPD) was performed on a Micromeritics AutoChem II 2920 analyzer to evaluate the acidity of Pt catalysts. Usually, 0.20 g of catalyst was loaded into a U-shaped quartz tube heated to 300 °C for 2 h (10 °C/min) under flowing helium (30 mL/min) to eliminate impurities and then cooled to 100 °C. Subsequently, a 10% NH_3/He gas mixture was introduced and maintained for 0.5 h for adsorption with a flowing rate of 30 mL/min, followed by purging with helium at the same temperature for 1.0 h to remove physically adsorbed NH_3. Lastly, the desorption profiles were recorded at 100−700 °C using a thermal conductivity detector (TCD). In addition, the acid types of series catalysts were tested adopting pyridine-adsorbed Fourier transformed infrared spectra (Py-IR) carried out on a Bruker TENSOR 27 spectrometer. Generally, 20 mg of sample was crushed into a self-supported wafer, immobilized into an IR cell, and *in situ* evacuated at 400 °C for 2 h. After being cooled to 50 °C, pyridine vapor was injected into the cell for saturation adsorption. Then, the Py-IR spectra were collected at 200 and 350 °C after the weakly adsorbed pyridine was removed under vacuum (<10^{-3} Pa) conditions. Finally, the Brønsted acid sites (BAS, C_B) and Lewis acid sites (LAS, C_L) were attained based on the formulas (1−2) described in the literature.[41]

$$C_B = \frac{1.88 IA_B R^2}{W} \tag{1}$$

$$C_L = \frac{1.42 IA_L R^2}{W} \tag{2}$$

where IA_B and IA_L (cm^{-1}) are the integral absorbance of BAS and LAS, respectively, R (cm) is the diameter of wafer, W (g) is the sample mass, and 1.88 and 1.42 ($\mu mol \cdot cm^{-1}$) are the integral extinction coefficients of BAS and LAS, respectively.

2.4. Catalytic Evaluation. The hydroconversion experiments of PHE on as-synthesized Pt/zeolite catalysts were executed in a stainless-steel downflow fixed-bed microreactor (ShanghaiYanzheng Experimental Instrument Co., Ltd., 10 mm ID, Length = 60 cm). Typically, 1.0 g of Pt catalyst (380−550 *μ*m) was diluted to 4.0 mL with SiC, fixed in the middle of the reactor using quartz wool, and then activated *in situ* at 450 °C for 2.5 h under 40 bar of hydrogen pressure with a flowing rate of 200 $mL \cdot min^{-1}$. Subsequently, 2.0 wt % PHE in *n*-octane solution was adopted as feedstock. The reactions were carried out at 180−280 °C under a hydrogen pressure of 40 bar with a weight hourly space velocity (WHSV) of 8.4 h^{-1} and H_2/oil of 500 N $mL \cdot mL^{-1}$. After reaction, liquid products were collected by a gas−liquid separation tank. The acquired effluents were divided into the following six categories (Figure 2): (i) partial hydrogenation products of PHE (PTP), (ii) perhydrophenanthrene stereoisomers (PHP), (iii) skeletal isomers of PHP (PSI), (iv) substituted alkyladamantanes with the same mass as PHP (PSA), (v) selective ring-opening products with one or two alkyl-rings of PHP opened (SRO), and (vi) cracking products with the mass less than PHP (CP). Moreover, a comprehensive two-dimensional gas chromatography−mass spectrometry facility (GC × GC-MS/FID, Shimadzu QP2010

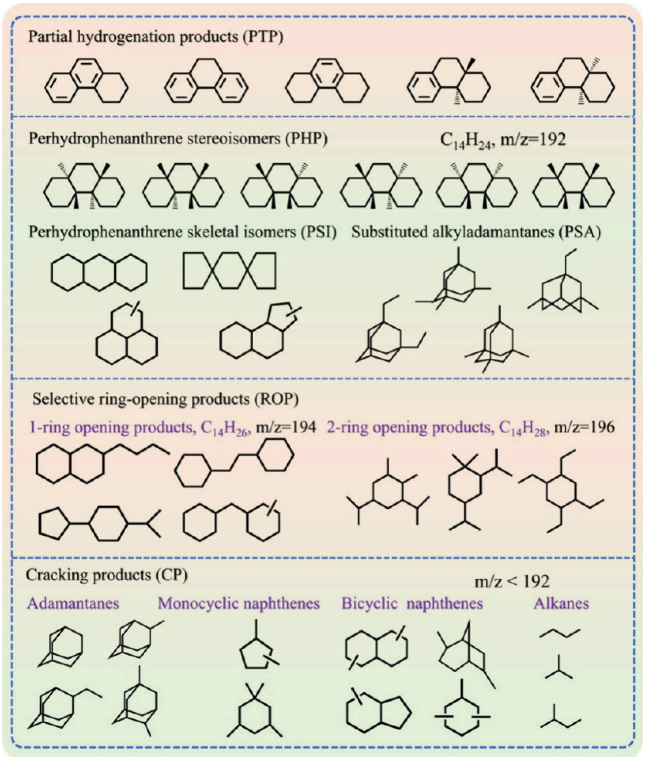

Figure 2. Molecule families and representative compounds of reaction products for phenanthrene hydroconversion.

https://doi.org/10.1021/acs.energyfuels.5c02305
Energy Fuels 2025, 39, 12551−12568

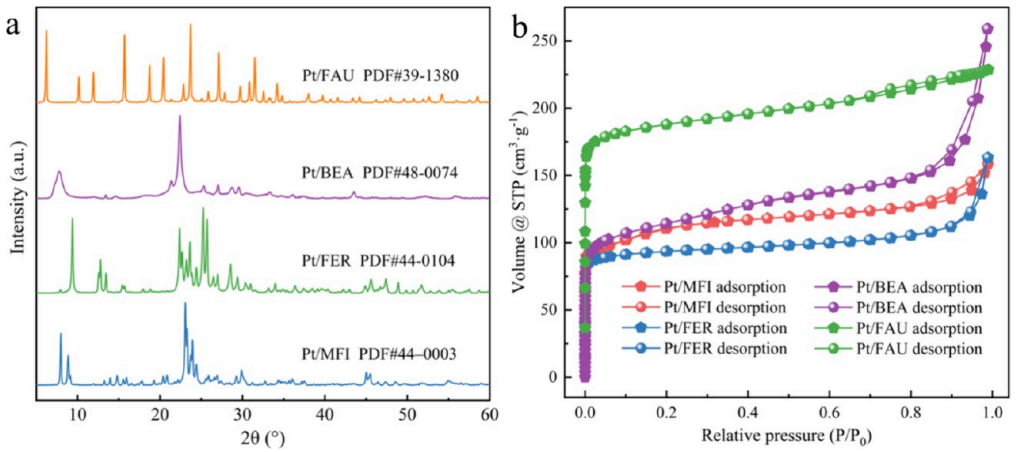

Figure 3. (a) XRD patterns and (b) nitrogen adsorption−desorption isotherms of Pt/MFI, Pt/FER, Pt/BEA, and Pt/FAU catalysts.

Ultra) was used to identify and quantify the products. During the analysis, a DB-1MS capillary column (30 m × 0.25 mm × 0.25 μm) was employed first to separate the liquid sample, and then the effluent was controlled by Zoex ZX1 thermal modulator into the secondary column (DB-17MS, 1.5 m × 0.10 mm × 0.10 μm). The modulation period was set to 5 s, the compounds separated by the columns were monitored via FID and MS detectors, and the signals were recorded at m/z range of 40−300. Data processing of GC × GC-MS and GC × GC-FID were conducted with GC image R2.5 software, and NIST 14 database was used to distinguish the molecule families of hydroconversion products.

2.5. Monte Carlo Simulation. To further illustrate the formation pathways of PSA and SRO species, the sorption isotherms and adsorption configurations of PHE and PHP in diverse zeolites were simulated via using the Monte Carlo strategy implemented on the Sorption module. A temperature range of 100−400 °C was adopted with equilibration steps set to 100000. The configurational bias method and COMPASSIII force field were applied for the guest molecule and zeolites. Electrostatic and van der Waals interactions were managed utilizing Ewald- and Atom-based methods, respectively, and the charges were endowed through using a force field assigned strategy. Besides, the adsorption configurations of guest compounds in zeolites were evaluated at a fixed pressure of 30 kPa and a temperature of 200 °C. Fine computational precision was employed in all calculations.

2.6. Fuel Properties Measurement. The density of as-synthesized HEAFs was determined using a Mettler Toledo DE40 density meter based on the ASTM D4052 standard. An IKA-C6000 isoperibol package 2/10 calorimeter was utilized to measure the volumetric net heat of combustion (VHOC) according to ASTM D240-02, and the numerical method is shown in formula 3.

$$Q_n(net, 25°C) = Q_g(gross, 25°C) - 0.2122 \times H \quad (3)$$

where $Q_n(net,25\ °C)$ and $Q_g(gross,25\ °C)$ (MJ/kg) are the total heat of combustion and net heat of fuel combustion, respectively, while H (wt %) is the hydrogen content of the prepared fuel.

The combustion quality and ignition delay time of synthesized fuel were evaluated in hot-plate ignition equipment. As shown in Figure S1, the hot-plate fabricated by Al_2O_3 was put in the center of a muffle furnace, and the temperature was detected through a thermocouple fixed on the surface of the plate. Typically, the hot-plate was heated to 400 °C, and then a 12 μL fuel droplet made by a pipetting gun was dropped into the plate. The combustion process was recorded using a FASTCAM UX50-type 160 K-CGB high-speed camera equipped with a Nikon AF NIKKOR camera lens at the shooting speed of 1000 images per second. Ignition delay time was calculated by the time difference between the occurrence of the flame and the initial fuel droplet contacting the hot-plate.

3. RESULTS AND DISCUSSION

3.1. Catalysts Properties. The XRD patterns of the as-synthesized highly dispersed Pt/zeolite catalysts are depicted in Figure 3a. All the samples displayed excellent zeolite crystallinity with no detectable impurities, and typical characteristic diffraction peaks of MFI (PDF#44-0003), FER (PDF#44-0104), BEA (PDF#48-0074), and FAU (PDF#39-1380) topological architectures were clearly observed on the patterns of Pt/MFI, Pt/FER, Pt/BEA, and Pt/FAU catalysts, respectively.[30,42−44] Besides, the typical peaks associated with Pt species (PDF#04-0802) were not monitored, indicating the superior metal dispersion on these acidic zeolites. This is beneficial for providing more active sites and enhancing the synergistic ability between metal and acidic sites in the hydroconversion reaction. In addition, all the Pt/zeolite catalysts in Figure 3b illustrated classical type-I isotherms without obvious hysteresis loops at relative pressure of 0.45, suggesting the microporous characteristics and the absence of mesopores.[45] The dramatic uptake at $P/P_0 < 0.02$ belonged to the adsorption of nitrogen in the micropores of zeolite, in which the Pt/FAU catalyst exhibited the largest adsorption quantity ascribed to its greater pore size (0.74 × 0.74 nm) and luxuriant micropores. Tiny hysteresis loops were discovered at P/P_0 = 0.7−1.0, attributed to the intercrystalline mesopores formed by the accumulation of zeolite particles.[46,47] Interestingly, the Pt/BEA catalyst exhibited a maximal adsorption amount of 259 $cm^3 \cdot g^{-1}$ at P/P_0 = 0.99, implying the supreme total pore volume among the Pt/zeolite catalysts. Furthermore, the textural properties were determined on account of the isotherms; as illustrated in Table 1, the specific surface area (S_{BET}) lowered in the order of Pt/FAU (748 $cm^3 \cdot g^{-1}$) > Pt/BEA (425 $cm^3 \cdot g^{-1}$) > Pt/MFI (402 $cm^3 \cdot g^{-1}$) > Pt/FER (371 $cm^3 \cdot g^{-1}$). The largest external specific surface area ($S_{ext.}$) of

Table 1. Textural Properties of Pt/MFI, Pt/FER, Pt/BEA, and Pt/FAU Catalysts

	Specific surface area ($m^2 \cdot g^{-1}$)			Pore volume ($cm^3 \cdot g^{-1}$)		
Catalysts	S_{BET}	$S_{micro.}$	$S_{ext.}$	V_{total}	$V_{micro.}$	$V_{ext.}$
Pt/MFI	402	367	35	0.2451	0.1610	0.0841
Pt/FER	371	337	34	0.2524	0.1300	0.1224
Pt/BEA	425	267	158	0.4006	0.1080	0.2926
Pt/FAU	748	682	66	0.3537	0.2660	0.0877

https://doi.org/10.1021/acs.energyfuels.5c02305
Energy Fuels 2025, 39, 12551−12568

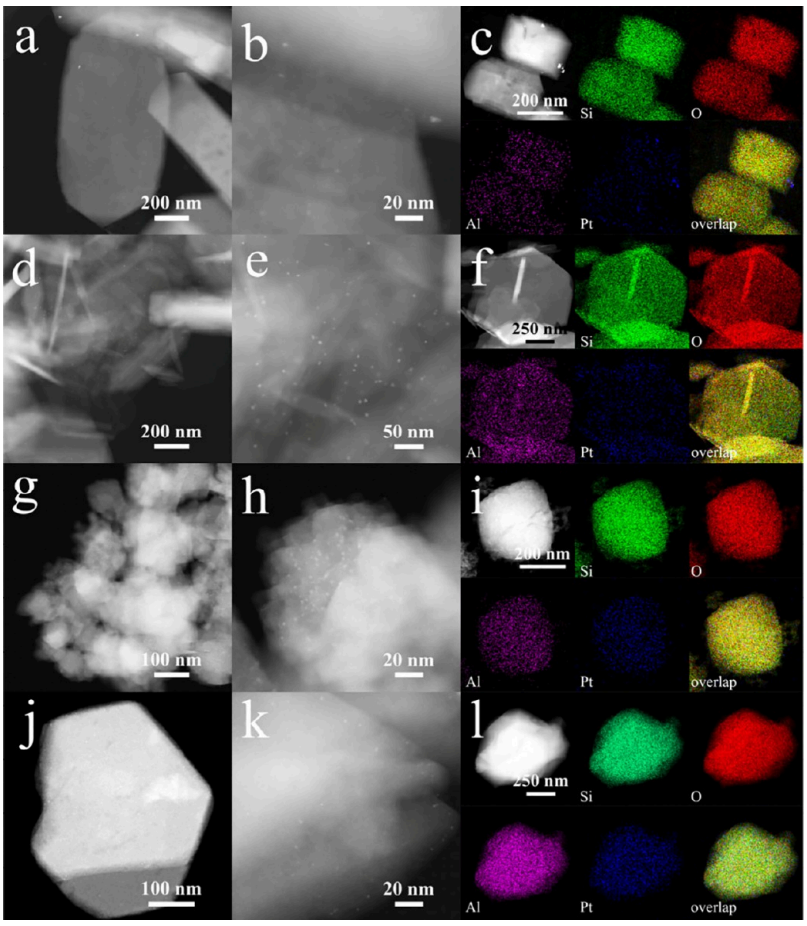

Figure 4. Field emission transmission electron microscopy (FETEM), high resolution transmission electron microscopy (HRTEM), and elemental mapping images of (a, b, c) Pt/MFI, (d, e, f) Pt/FER, (g, h, (i) Pt/BEA, and (j, k, l) Pt/FAU catalysts.

158 $cm^3 \cdot g^{-1}$ and total pore volume (V_{total}) of 0.4006 $cm^3 \cdot g^{-1}$ were acquired on the Pt/BEA catalyst. Besides, Pt/MFI and Pt/FER presented a similar distribution of pore volume.

Figure 4 depicts the morphology of zeolite supports and particle size distribution of loaded active metal Pt. In Figure 4a, a representative coffin-like appearance was observed for Pt/MFI catalyst, which had been often reported in the literature.[42,48] Evidently, inhomogeneous distribution of Pt species on the MFI zeolite and greater Pt particles constituted by agglomeration were found, meaning inferior metal−support interactions and the occurrence of sintering during calcination. The HRTEM image in Figure 4b manifested that the average size of Pt particles was approximately 2.6 nm except for those agglomerated particles. Additionally, striking Pt particles were detected in the HAADF-STEM image of Pt/MFI, and the mapping images (Figure 4c) further verified better dispersion of Pt substances than the catalyst prepared by an impregnation method.[38] For the Pt/FER catalyst (Figure 4d-e), it presented a layered morphology of FER zeolite and decent metal distribution with a mean size of 4.3 nm. The larger size of Pt species in Pt/FER can be ascribed to smaller pore diameter of 0.35 × 0.48 and 0.42 × 0.54 nm, which is smaller than the kinetic diameter of $Pt(NH_3)_4^{2+}$ cations (0.48 nm).[49] Consequently, the Pt species were mainly distributed on the external surface of FER zeolite and agglomerated due to Ostwald ripening during the preparation process. The mapping images in Figure 4f also could indicate the superior distribution of Pt throughout FER zeolite. Differently, no distinct morphologies could be investigated for the BEA zeolite, emerging irregular shapes (Figure 4g). Prominent dispersion of Pt particles with a mean size of 2.0 nm was spread over the BEA zeolite (Figure 4h-i), suggesting strong metal−support interactions. Analogously, the dispersion of Pt was further intensified on the Pt/FAU catalyst with the smallest average size of 1.6 nm (Figure 4k). Moreover, it also exhibited the classical appearance of faujasite in the FAU zeolite.[50] Distinctly, all the Pt/zeolite catalysts prepared through an enhanced strong electrostatic adsorption method exhibited decent metal dispersion than the impregnation method, consistent with our previous works.[38,51] However, due to the effect of the zeolite topology, there were differences in the dispersion of the series of bifunctional Pt/zeolite catalysts. In summary, the dispersion of Pt particles decreased in the following order: Pt/FAU > Pt/BEA > Pt/MFI > Pt/FER. Furthermore, the Si/Al ratios and actual Pt loading of as-prepared catalysts were determined by ICP-OES, with the data compiled in Table 2. All catalysts presented a consistent Pt loading value of about 1.80 wt %, in line with the theoretical loading. Based on the reports,[52,53] higher aluminum content in acid zeolites is beneficial to boost the dispersion of supported metals owing to the Al−Pt interactions. The Pt/MFI and Pt/BEA displayed similar Si/Al ratios. Consequently, the superior metal dispersion of the Pt/BEA catalyst could be attributed to its larger pore size and stronger interactions. Meanwhile, Pt/FAU possessed the minimal Si/Al ratio of 2.7, which correlates with the metal dispersion presented in Figure 4. The largest

https://doi.org/10.1021/acs.energyfuels.5c02305
Energy Fuels 2025, 39, 12551−12568

Table 2. Si/Al Ratios, Pt Loading, and Quantitative Acidic Sites of Pt/MFI, Pt/FER, Pt/BEA, and Pt/FAU Catalysts

			Peak Temperature (°C)[b]		Acidic sites (mmol·g^{-1})[b]		
Catalysts	Si/Al ratios[a]	Pt loading (wt%)[a]	LTP	HTP	weak	strong	total
Pt/MFI	21.3	1.79	310	542	0.729	0.528	1.257
Pt/FER	32.6	1.80	283	555	0.690	0.285	0.976
Pt/BEA	19.8	1.78	250	487	0.925	0.609	1.534
Pt/FAU	2.7	1.79	248	436	1.576	1.003	2.579

[a]Determined by ICP-OES measurements. [b]Deconvolution on the basis of NH_3-TPD profiles.

pore dimension (0.74 nm) and larger Al concentration strengthened the metal−support interactions, thus facilitating the splendid dispersion of active metal Pt in the zeolite.

The NH_3-TPD profiles of Pt/MFI, Pt/FER, Pt/BEA, and Pt/FAU catalysts are plotted in Figure 5, while Table 2 shows

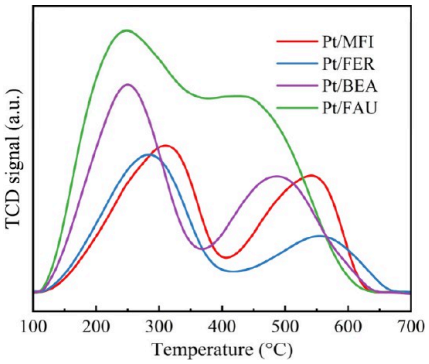

Figure 5. NH_3-TPD profiles of Pt/MFI, Pt/FER, Pt/BEA, and Pt/FAU catalysts.

the quantitative acidic sites. As exhibited in Figure 5, two well-resolved shoulder peaks appeared for all of the Pt samples. The low-temperature desorption peaks (LTP) at 248−310 °C were ascribed to the weak acidic sites, while the high-temperature desorption peaks (HTP) situated at 436−555 °C were assigned to strong acid sites.[54] Among the Pt catalysts, Pt/FAU showed the greatest NH_3 desorption amount because of the luxuriant Al species in the FAU zeolite, as determined by ICP-OES (Table 2). Additionally, different desorption temperatures of LTP and HTP reflected the strength of the acidic sites in the catalysts. Higher desorption peak temperatures indicate a stronger acid. On account of the data in Table 2, Pt/FAU exhibited the most acidic sites of 2.579 mmol·g^{-1}, which was 1.6, 2.1, and 2.6 times greater than that of Pt/BEA, Pt/MFI, and Pt/FER catalysts, respectively. This trend is consistent with the Al contents in diverse Pt/zeolite catalysts. A higher number of acidic sites is profitable to promote metal dispersion and boost isomerization and selective ring-opening reactions for selective hydroconversion of PAHs.[29,55]

The Brønsted (B) and Lewis (L) acid sites in the as-prepared Pt catalysts were further estimated employing pyridine-adsorbed infrared spectroscopy (Py-IR). Besides, the Py-IR spectra recorded at 200 and 350 °C reflected the total and strong B/L acid sites, respectively. The weak B/L acid sites were calculated by subtracting strong acid sites from the total acid sites. As demonstrated in Figure 6, the vibrational bands at 1452 and 1542 cm^{-1} corresponded to the diagnostic fingerprints of B and L acid sites respectively, while the band at 1489 cm^{-1} was attributed to the combined action of both acid types.[56] It could be distinctly observed that Pt/FAU exhibited the strongest vibrational bands of B and L acid sites, while the weakest one was acquired on Pt/FER catalyst, agreeing with the NH_3-TPD results (Figure 5). Differently, Pt/BEA delivered a stronger adsorption band for L compared to B acid, suggesting that L acid was predominant in the catalyst. Similarly, the other Pt catalysts presented a higher concentration of B acid sites at both 200 and 350 °C. Furthermore, the quantitative values of B and L acid were calculated according to the empirical equation.[41] As displayed in Table 3, the total number of B acid sites reduced in the order Pt/FAU (1356.62 μmol·g^{-1}) > Pt/BEA (629.11 μmol·g^{-1}) > Pt/MFI (477.77 μmol·g^{-1}) > Pt/FER (260.62 μmol·g^{-1}). All catalysts exhibited significantly higher amounts of B acid than L acid except for the Pt/BEA catalyst. In addition, Pt/FAU also showed the largest total B to L acid ratio (B_T/L_T) of 2.09 and strong B to L acid ratio (B_S/L_S) of 2.54, which were much higher than those of the other Pt/zeolite catalysts. B acid plays a crucial role in the one-step hydroconversion of PAHs; it can facilitate the hydrosaturation of aromatics and the rearrangement of saturated cycloalkanes, thereby accelerating the isomerization and selective ring-opening reactions.[55,57] However, excessively strong acidic sites can also promote undesirable cracking reactions, which may reduce the yield of target HEAFs products.

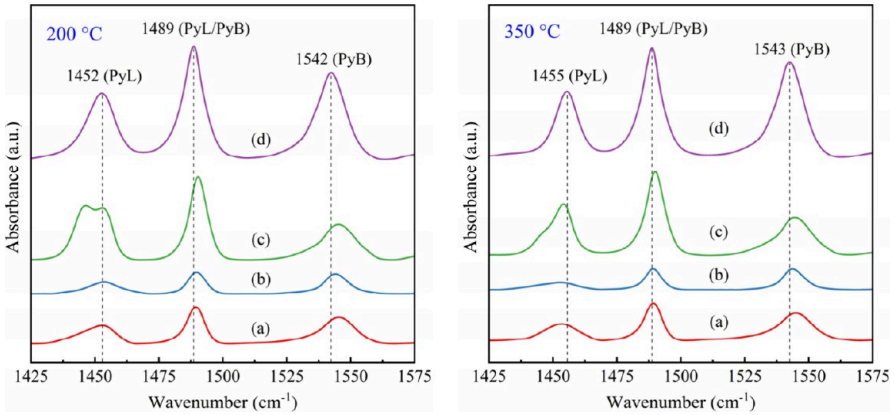

Figure 6. Pyridine adsorption infrared spectra of (a) Pt/MFI, (b) Pt/FER, (c) Pt/BEA, and (d) Pt/FAU catalysts at 200 and 350 °C, respectively.

https://doi.org/10.1021/acs.energyfuels.5c02305
Energy Fuels 2025, 39, 12551−12568

Table 3. Quantitative Data on Acid Types Derived from Pyridine Adsorption Infrared Spectra

	Brønsted acid sites (μmol·g^{-1})			Lewis acid sites (μmol·g^{-1})				
Catalysts	Total[a]	Weak[b]	Strong[c]	Total[a]	Weak[b]	Strong[c]	B_S/L_S[d]	B_T/L_T[d]
Pt/MFI	477.77	36.24	441.53	228.42	54.50	173.92	2.54	2.09
Pt/FER	260.62	52.91	207.71	139.13	52.36	86.77	2.39	1.87
Pt/BEA	629.11	75.11	554.00	684.29	274.93	409.36	1.35	0.92
Pt/FAU	1356.62	142.66	1213.96	774.90	223.87	551.03	2.20	1.75

[a]The total amount sites of Brønsted acid and Lewis acid calculated using band at 1540 cm^{-1} and 1450 cm^{-1}, respectively, by Py-IR at 200 °C. [b]Calculated using Weak = Total − Strong. [c]The strong amount sites of Brønsted acid and Lewis acid calculated using band at 1540 cm^{-1} and 1450 cm^{-1}, respectively, by Py-IR at 350 °C. [d]S and T represent strong and total amount of acid sites, respectively.

3.2. Selective Hydroconversion of Phenanthrene into High-Density Endothermic Aviation Fuels. A down-flow fixed-bed microreactor was employed to carry out the selective hydroconversion of PHE into HEAFs, executed over a temperature range of 180−280 °C and under hydrogen pressure of 40 bar with WHSV of 8.4 h^{-1}. The formation pathways of PSA and SRO were investigated extensively using supported highly dispersed Pt catalysts supported on diverse topological zeolites. Figure 7 plots the conversion of PHE at various temperatures over the as-prepared bifunctional Pt/zeolite catalysts. For Pt/FER catalyst, the PHE conversion was 83.0% at a low temperature of 180 °C, showing the worst catalytic activity among all catalysts, and a high temperature of 240 °C was required to achieve nearly complete conversion of PHE. In addition, the Pt/MFI exhibited decent catalytic properties, achieving better conversion of 96.3% at identical conditions and reaching 100% at 200 °C. Interestingly, entire conversions were observed at all the employed temperatures for both Pt/BEA and Pt/FAU catalysts. On account of the FETEM, NH_3-TPD, and Py-IR data, Pt/FER possessed the largest particle size of Pt particles and the fewest acid sites. Most importantly, the kinetic diameter of PHE is 0.70 nm, which exceeds the porous framework of FER (0.42 × 0.54 nm, 0.35 × 0.48 nm).[58] As a result, the selective hydroconversion of PHE primarily occurred on the external surface. Therefore, Pt/FER demonstrated the poorest catalytic performance. Notably, although the pore size of Pt/MFI catalyst (0.51 × 0.55 nm, 0.53 × 0.56 nm) is also smaller than the kinetic diameter of PHE, it had more acid sites, which can boost the additional hydrogenation pathways by spillover hydrogen.[59] In consequence, the catalytic activities of Pt/MFI were strengthened compared to the Pt/FER catalyst. Furthermore, Pt/BEA and Pt/FAU catalysts illustrated much higher acid densities, and their suitable pore diameters (0.66 × 0.77 nm and 0.56 × 0.56 nm for BEA, and 0.74 × 0.77 nm for FAU)

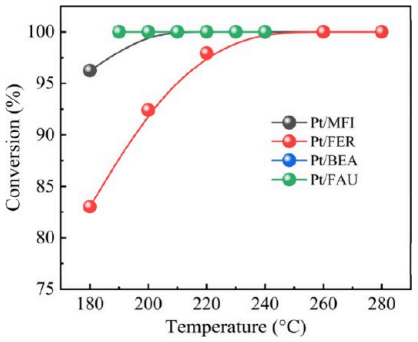

Figure 7. Conversion of phenanthrene as a function of temperature over diverse bifunctional Pt/zeolite catalysts. Reaction conditions: P = 40 bar, WHSV = 8.4 h^{-1}, H_2/oil = 500 N mL/mL.

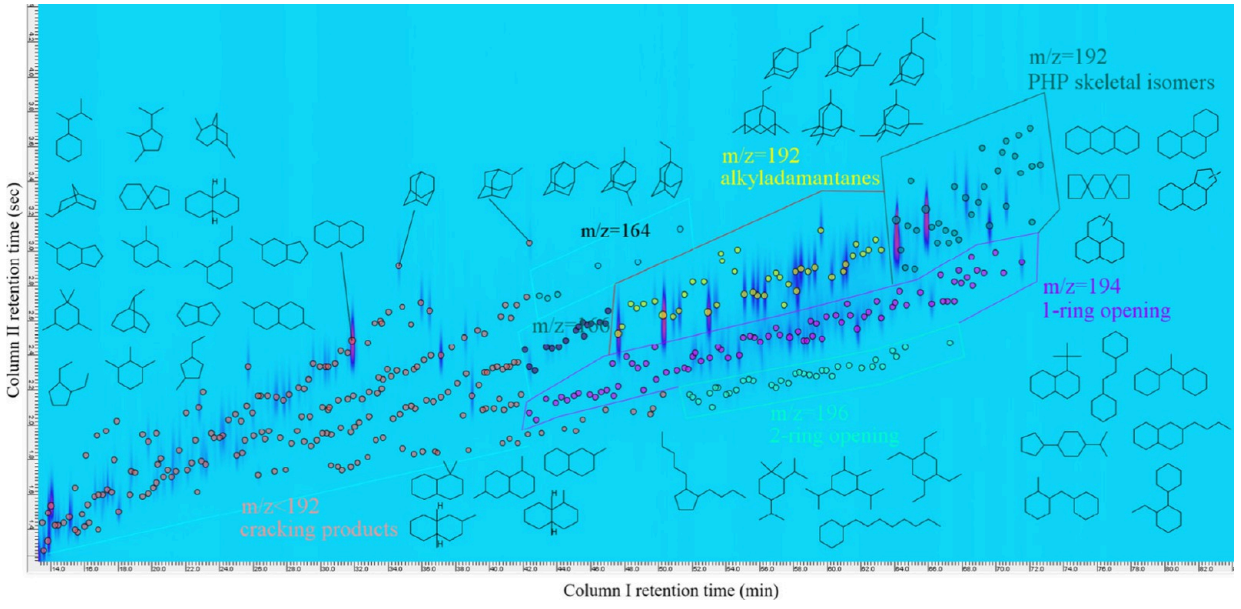

Figure 8. Comprehensive GC×GC-MS chromatography of liquid products of phenanthrene hydroconversion.

https://doi.org/10.1021/acs.energyfuels.5c02305
Energy Fuels 2025, 39, 12551−12568

accelerated the diffusion of intermediate products. Therefore, conspicuous catalytic activities were obtained.

Analyzing the product distribution of PHE is critically important for understanding the selective hydroconversion routes. Due to the complexity of the effluents, comprising thousands of compounds, ordinary gas chromatography (GC) is insufficient for accurate identification. Hence, comprehensive 2D GC×GC-FID/MS equipment was employed to realize precise quantification of the reaction products. For instance, the perhydrogenation product of PHE, perhydrophenanthrene, has six stereoisomers, which exhibit excellent resolution on the GC×GC-FID chromatogram (Figure S2). In addition, the GC×GC-MS chromatogram of the liquid product obtained after the hydroconversion of PHE over the bifunctional Pt/zeolite catalyst is shown in Figure 8, where hundreds of species were detected. It is quite difficult to perform quantitative analysis for each product. The reaction products were divided into the following categories: (i) partial saturated products of PHE hydroconversion (PTP), including dihydrophenanthrene (DHP), tetrahydrophenanthrene (THP), and octahydrophenanthrene (OHP); (ii) six stereoisomers of perhydrophenanthrene (PHP); (iii) skeletal isomers of PHP (PSI), for instance, perhydroanthracene, dispiro[4.2.4^8.2^5]tetradecane; (iv) alkyladamantanes with the same molecular formula as PHP (PSA); (v) selective ring-opening products with one or two alkyl-rings of PHP opened (SRO); and (vi) cracking products (CP). As exhibited in Figure 8, the retention times of PSA and SRO substances significantly overlap in the first dimension, whereas effective separation is achieved in the second dimension. Furthermore, the corresponding 3D view of the GC×GC-FID chromatogram showed that PSA was the dominant product (Figure 9). This further confirmed that GC×GC-MS/FID chromatography is the effective analysis method to identify the tanglesome effluents of PHE hydroconversion.

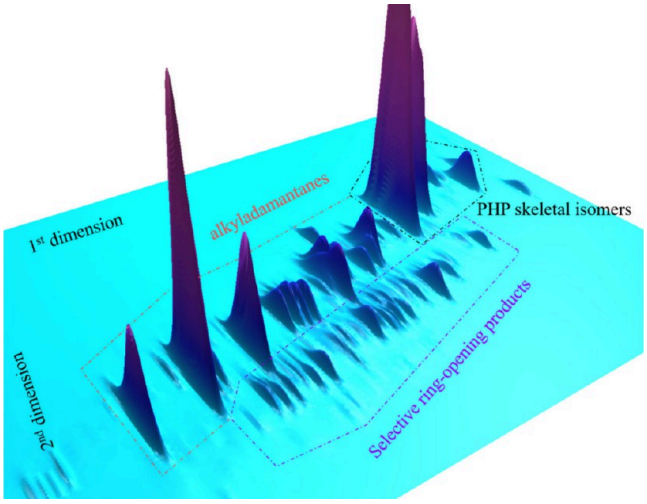

Figure 9. 3D view of the comprehensive GC×GC-FID chromatogram of liquid products of phenanthrene hydroconversion.

Figure 10 summarizes the product distributions of PHE hydroconversion over various Pt/zeolite catalysts at temperatures ranging from 180 to 280 °C. As described in Figure 10a, Pt/MFI exhibited commendable deep hydrosaturation activity, with yields of PHP and PTP at 94.0 and 3.5 wt %, respectively, at a relatively low temperature of 180 °C. However, the yields of PSA and SRO products were negligible. Meanwhile, a PSI yield of 1.0 wt % was detected on the Pt/MFI. As the temperature elevated to 240 °C, the yield of PHP gradually decreased to 88.8 wt %, followed by a more pronounced drop to 58.9 wt % at 280 °C. Concurrently, the yields of PSI and CP steadily increased to 15.0 and 22.6 wt %, respectively. Unfortunately, the yields of PSA and SRO exhibited only a slight increase with the rising temperature. This indicated that Pt/MFI possessed limited isomerization and selective ring-opening activities. The rise in reaction temperature primarily enhanced the isomerization of PHP, leading to the generation of PSI and promoting cracking over the Pt/MFI catalyst. From Figure 10b, Pt/FER exhibited worse catalytic properties than the Pt/MFI catalyst. A 90.2 wt % yield of PTP was obtained at 180 °C, which was 86.7 wt % higher than that of Pt/MFI. Only 9.2 wt % of PHP was gained at the identical conditions, presenting inferior deep hydrosaturation ability. The yield of PHP attained the maximal value of 84.5 wt % as the temperature rose to 240 °C. Similar to the Pt/MFI catalyst, Pt/FER also did not convey decent isomerization and ring-opening activity. The elevated temperature mainly promoted the skeletal isomerization of PHP into PSI. Additionally, Pt/FER depicted smaller yield to CP, with only 7.9 wt % at 280 °C. which could be attributed to the fewer acid sites than Pt/MFI (Figure 5). A higher concentration of acid sites is known to promote cleavage reactions.[60] It is evident that perhydrogenated PHP was the primary product over MFI and FER supported Pt catalysts. Fortunately, Pt/BEA and Pt/FAU showed superior deep hydrosaturation, isomerization, and selective ring-opening properties. Notably, at lower temperatures, PTP was not found in the products, indicating exceptional hydrosaturation performances. For Pt/BEA catalyst, the yields of PHP, PSI, and PSA at 180 °C were determined at 86.8, 9.8, and 1.0 wt %, respectively. Afterward, with elevating temperature, the yield of PHP continued to reduce, attaining the minimal yield of 1.8 wt % at 280 °C. Conversely, PSI initially increased and subsequently decreased and reached the maximum of 27.1 wt % at 220 °C, which manifested that PSI was generated from the further conversion of PHP. Besides, PSA and SRO also presented improved yield with the advance of temperature, and the supreme yields of 26.9 and 13.9 wt % for PSA and SRO were both acquired at 230 °C. Additionally, it is noteworthy that at lower reaction temperatures, the yields of PSA and SRO species elevated with the rising yield of PSI. Upon achieving its maximum, the yields of PSA and SRO continued to reinforce before subsequently decreasing. This observation verified that PSA and SRO were primarily produced through the further reactions of PSI, rather than being directly derived from PHP. Importantly, a substantial amount of PSA and SRO products were generated on Pt/BEA compared to the Pt catalysts supported on MFI and FER zeolites. According to previous analyses, all three catalysts possessed abundant acidic sites and consistent metal loading. In consequence, the differences in catalytic activities were chiefly attributed to the topological structure of zeolites. BEA featured a larger three-dimensional pore size, which could boost the diffusion of intermediates into the pores and promote interaction with the abundant B acid sites, thereby facilitating skeletal rearrangement isomerization reactions, ultimately leading to the formation of PSA and SRO. Lastly, Pt/BEA also exhibited a larger yield to CP because it possessed stronger acid densities compared to Pt/MFI and Pt/FER catalysts. A significant amount of alkyladamantanes and alkyl

https://doi.org/10.1021/acs.energyfuels.5c02305
Energy Fuels 2025, 39, 12551−12568

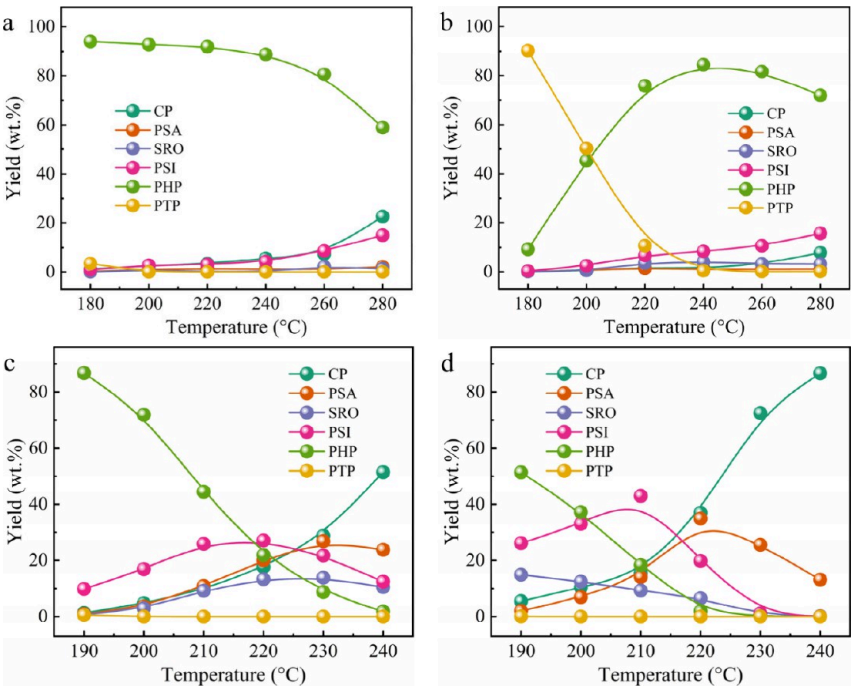

Figure 10. Product yield of PHE hydroconversion over (a) Pt/MFI, (b) Pt/FER, (c) Pt/BEA, and (d) Pt/FAU catalysts. (Reaction conditions: P = 40 bar, WHSV = 8.4 h^{-1}, H_2/oil = 500 N mL/mL).

Table 4. Comparison of Yields and Hydroconversion Conditions of PSA and SRO from Tricyclic Hydrocarbons with Those Reported in Literature

Reactants	Catalysts	Reactor	WHSV (h^{-1})	Pressure (bar)	Temperature (°C)	Yield (wt %)		References
						PSA	SRO	
fluorene	Pt/USY	fixed-bed	-	30	260	2	-	34
	Pt/HY			30	260	7		
	Pt/MY			30	260	9		
	Pt/Beta			30	260	0		
	Pt/ASA			30	260	0		
perhydrophenanthrene	Pt/USY	fixed-bed	1−10	60	280	6	8	32
	Pt/Beta	fixed-bed	1−10	60	280	8	-	33
	Pt/ASA			60	280	0		
	Pt/USY			60	280	18		
perhydrofluorene	Pt/Beta	fixed-bed	1−4	25	305	3	-	67
	Pt/USY			25	320	27		
	Pt/USY			40	280	6.1		
	Pt/0.05-USY	batch	-	40	280	5.6	-	36
	Pt/0.1-USY			40	280	2.3		
	Pt/H-β	fixed-bed	0.5	60	300	-	-	11
	Pt/USY			60	260	19		
phenanthrene	Pt/0.05M-USY	batch	-	60	260	32	-	35
	Pt/0.1M-USY			60	260	28		
	Pt/BEA	fixed-bed	8.4	40	230	26.9	13.9	this work
			8.4	40	220	34.9	6.5	
	Pt/FAU		14.7	40	240	39.0	2.0	
			21.0	40	240	36.5	6.1	

substitutional polycycloalkanes with carbon loss were detected in the CP product, indicating that PSA and SRO species were subject to further cracking. To differentiate, the alkyladamantanes and alkyl substitutional polycycloalkanes created by the cracking reactions were denoted as cPSA and cSRO, respectively. Excitedly, Pt/FAU showed optimal catalytic activities for isomerization and selective ring-opening of PHE (Figure 10d). Under identical conditions, Pt/FAU presented higher yields to PSI, SRO, and PSA compared to the Pt/BEA catalyst, demonstrating its excellent properties for selective hydroconversion of PHE. The supreme yields of 42.9, 14.9, and 34.9 wt % for PSI, SRO, and PSA were gained at 210 °C, 190, and 220 °C, respectively. After Pt/BEA and Pt/FAU catalysts were compared, it could be confirmed that Pt/FAU could acquire higher yields to isomerization and selective ring-opening products at lower reaction temperatures. Conse-

https://doi.org/10.1021/acs.energyfuels.5c02305
Energy Fuels 2025, 39, 12551−12568

quently, Pt/FAU is the favored bifunctional catalyst for the hydroconversion of PHE to produce HEAFs. The outstanding catalytic activity of Pt/FAU could be attributed to a larger pore size than BEA, which resulted in weakened diffusion resistance for intermediates within the FAU architecture. Particularly, the presence of supercages with dimensions of 1.25 nm provides a more favorable environment for the generation of PSA and SRO components. Furthermore, Pt/BEA and Pt/FAU illustrated significantly higher yields compared to those reported in the literature (Table 4), indicating that the use of an enhanced strong electrostatic adsorption method significantly promoted the synergistic interaction between the metal and acidic sites, and the highly dispersed Pt clusters were beneficial to enhance the yield of HEAFs.

As reported,[5,61] alkyladamantanes have higher density, better heat stability, larger volumetric net of combustion, and superior thermal oxidation stability, which are the main components of modern high-density endothermic aviation fuel. To elucidate the formation mechanism of PSA, it is essential to analyze the variation trends of PSA over different Pt/zeolite catalysts. On the basis of the qualitative GC×GC-FID/MS measurement data, 1,3,5,6-tetramethyladamantane (1,6-TMA), 1,3,5,7-tetramethyl-adamantane (1,7-TMA), 1,3-diethyladamantane (1,3-DEA), and 1,3-dimethyl-5-ethyladamantane (1,5-DMA) were identified as the dominating components in PSA, formed without carbon loss during the one-step selective hydroconversion of PHE. Figure 11

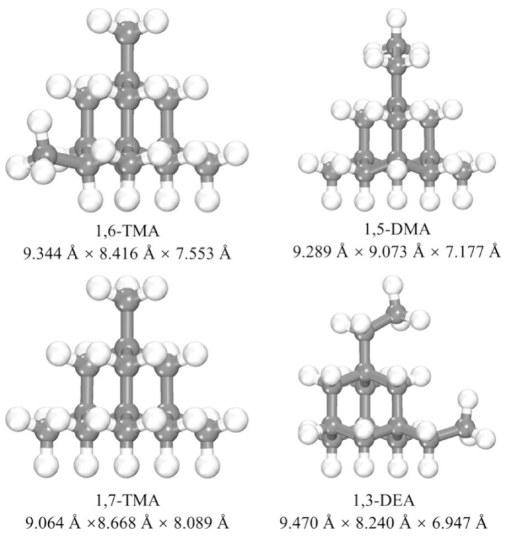

Figure 11. Optimized structural configurations and 3D size of alkyladamantane. (1,6-TMA: 1,3,5,6-tetramethyladamantane, 1,5-DMA: 1,3-dimethyl-5-ethyladamantane, 1,7-TMA: 1,3,5,7-tetramethyl-adamantane, 1,3-DEA: 1,3-diethyladamantane).

describes the optimized configurations and three-dimensional size of PSA, calculated using VASP software. The PSA yields over the prepared Pt catalysts were analyzed, and the formation pathways were carefully considered.

Figure 12 exhibits the variation in the PSA yield at different temperatures. For Pt/MFI catalyst, 1,7-TMA was the dominating product from 180 to 260 °C, with the largest yield of 0.8 wt % observed at 220 °C. Second, the yield to 1,6-TMA gradually improved with rising temperatures, reaching 0.3 wt % at 280 °C, indicating that higher temperature mainly boosted the conversion of PSI to 1,6-TMA. Inversely, the yields of 1,5-DMA and 1,3-DEA did not change much as the temperature increased. In Figure 12b, Pt/FER also exhibited a relatively inferior yield to PSA. The maximal yields of 1,6-TMA (0.5 wt %) and 1,7-TMA (0.7 wt %) were attained at 220 °C. No clear regularity was monitored on the yields of 1,5-DMA and 1,3-DEA, likely due to the difficulty in accurately quantifying these low-yield substances. Additionally, it is important to note that the dimensions of PHE and PSA are greater than the pore size of MFI and FER. Therefore, the one-step hydroconversion of PHE and the formation of PSA primarily occurred on the external surface, leading to the uneven distribution of PSA. Excitingly, plentiful PSA were detected on Pt/BEA and Pt/FAU catalysts. For Pt/BEA in Figure 12c, the yield of all PSA species increased as the temperature rose from 190 to 230 °C, followed by a reduction due to cleavage reactions. At 230 °C, the yields of 1,6-TMA, 1,5-DMA, 1,7-TMA, and 1,3-DEA were 3.6 wt %, 12.1, 4.4, and 6.7 wt %, respectively. The product distribution consistently followed the order of 1,5-DMA > 1,3-DEA > 1,7-TMA > 1,6-TMA, with 1,5-DMA and 1,3-DEA being the dominating species in PSA products. As for Pt/FAU catalyst, higher yields of diverse PSA species were observed under the same conditions. Differently, 1,6-TMA and 1,5-DMA were the main products. The largest yields of 1,6-TMA (10.3 wt %), 1,5-DMA (17.7 wt %), 1,7-TMA (3.8 wt %), and 1,3-DEA (3.0 wt %) were attained at 220 °C. Comparing the PSA yields on Pt/BEA and Pt/FAU catalysts, it is evident that Pt/FAU produced higher yields of 1,6-TMA and 1,5-DMA, while Pt/BEA exhibited higher yields of 1,7-TMA and 1,3-DEA. This disparity might be attributed to the fact that the stronger and more abundant acid sites of Pt/FAU facilitated further reactions.[62] It is significant to understand the formation pathways of PSA on prepared Pt catalysts. Understanding the formation pathways of PSA on prepared Pt/zeolite catalysts is crucial. The pore diameters decreased in the order of FAU > BEA > MFI > FER (Figure 1). Owing to the smaller pore sizes of MFI and FER, PHE cannot diffuse into their pores. Additionally, the Py-IR data in Figure 6 delivered that Pt/MFI possessed a larger B_T/L_T ratio compared to Pt/BEA (2.09 vs 0.92), yet only a trace amount of PSA was obtained from the Pt/MFI catalyst. In this case, increasing the reaction temperature predominantly promoted the cracking of PSI rather than the generation of PSA. In contrast, Pt/BEA exhibited a volcano-shaped distribution of PSA, highlighting that the accessible porous structure is a crucial factor influencing PSA formation and is essential for facilitating the skeletal rearrangement of PSI. As speculated, the PSA yields were significantly higher over Pt/FAU, suggesting that the reactions occurred within the pores of zeolites. It is well-known that the majority of acid sites are situated within the microporous channels of zeolites, while the outside surfaces display only a limited number of acid sites.[63,64] Hence, the acid sites in the micropores were not effectively utilized for the one-step hydroconversion of PHE, resulting in inferior PSA yields investigated for the Pt/MFI and Pt/FER catalysts. Furthermore, the SRO products on diverse Pt catalysts also exhibited a trend similar; that is, the SRO reaction was also mainly executed in micropores. In consequence, to reinforce the yields of PSA and SRO products in the one-step hydroconversion of PHE, strengthening the accessibility of acid sites within the porous channels of bifunctional Pt/zeolite catalysts is pivotal. 2-Methyldodecahydro-1*H*-phenalene (MDP) is the critical intermediate in the generation of PSA,[65] and it also was

https://doi.org/10.1021/acs.energyfuels.5c02305
Energy Fuels 2025, 39, 12551−12568

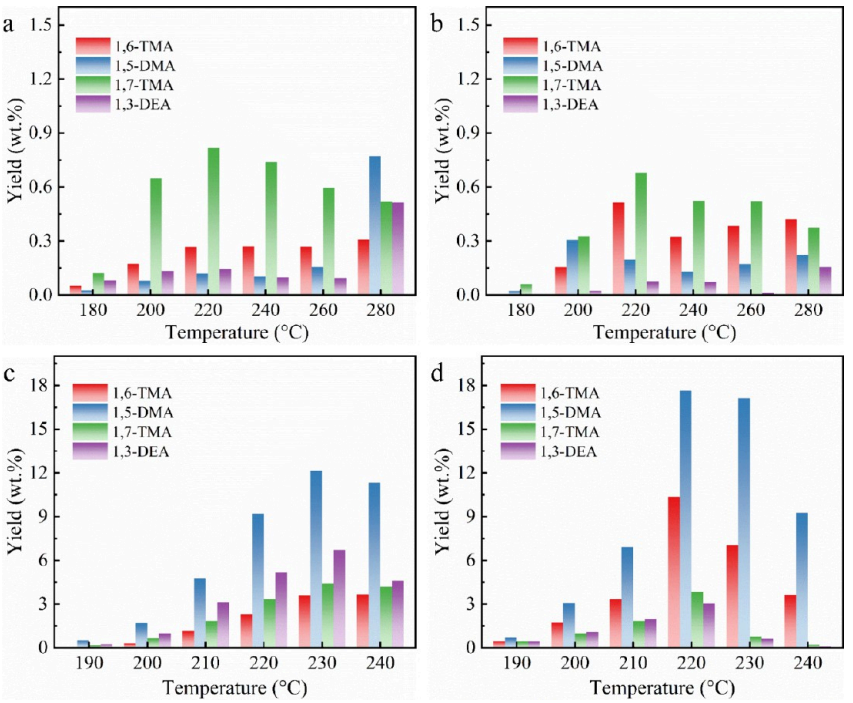

Figure 12. Alkyladamantane yield of PHE hydroconversion over (a) Pt/MFI, (b) Pt/FER, (c) Pt/BEA, and (d) Pt/FAU catalysts. (1,3,5,6-tetramethyladamantane: 1,6-TMA, 1,3-dimethyl-5-ethyladamantane: 1,5-DMA, 1,3,5,7-tetramethyl-adamantane: 1,7-TMA, 1,3-diethyladamantane: 1,3-DEA. Reaction conditions: P = 40 bar, WHSV = 8.4 h^{-1}, H_2/oil = 500 N mL/mL).

discovered in the PSI product on account of the GC×GC-MS data (Figure 8). Scheme 1 illustrates the formation route of

Scheme 1. Schematic Illustration of the Pathway for the Conversion of PHP into 1,6-TMA

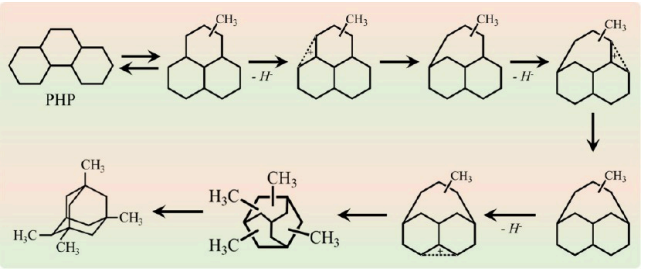

1,6-TMA via the hydroconversion of PHP. During the reaction, MDP is initially yielded by the cycloisomerization of PHP species, followed by a series of intricate rearrangement reactions of carbocations. This process involves dehydrogenation, rearrangement, ring opening, hydrogen transfer, and alkylation, among others. In addition, it also has been pointed out that 1,7-TMA shows better stability than 1,6-TMA owing to the highly symmetrical molecular configurations.[65,66] Different PSA substances are produced through the interconversion. The experimental data further indicated that 1,7-TMA compound was the predominant component in the PSA products obtained from Pt/MFI and Pt/FER. Furthermore, the inequitable PSA distributions over Pt/BEA and Pt/FAU could be attributed to the combined effects of acidic sites and porous architectures.

After analyzing the changing trends in hydrogenation products on diverse catalysts, the reaction pathways for hydroconversion of PHE are deduced in Scheme 2. In our previous studies,[17,38] the conversion routes involved in the

Scheme 2. Schematic Diagram of the Reaction Pathways for Phenanthrene Hydroconversion[a]

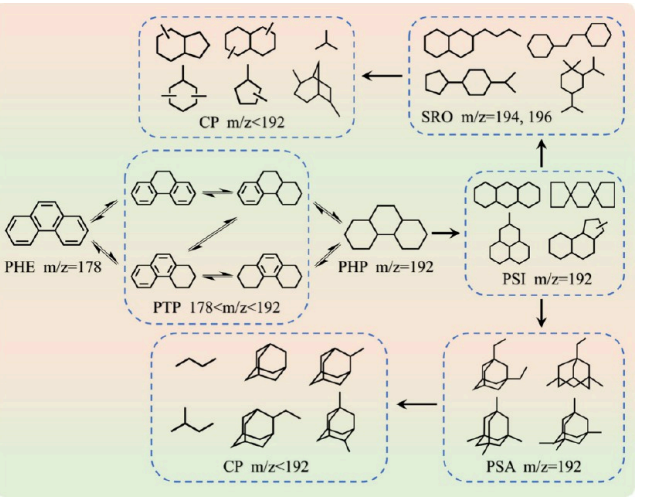

[a]PHE: phenanthrene, PTP: partial hydrogenation products of PHE, PHP: perhydrophenanthrene stereoisomers, PSI: skeletal isomers of PHP, PSA: alkyladamantanes with the same molecular formula as PHP, SRO: selective ring-opening products with one or two alkyl-rings of PHP opened, CP: cracking products.

hydrogenation of PHE to form PHP had been deeply understood. The variation of products with temperature on Pt/MFI and Pt/FER also corroborated the pathways of deep hydrosaturation. The three aromatic rings of PHE possess highly conjugated structures with substantial resonance energies and thermodynamic stability. Under the action of bifunctional Pt/zeolite catalysts, PHE was expected to primarily undergo hydrosaturation rather than hydrocracking and ring-opening reactions.[20] At lower temperatures, the

https://doi.org/10.1021/acs.energyfuels.5c02305
Energy Fuels 2025, 39, 12551−12568

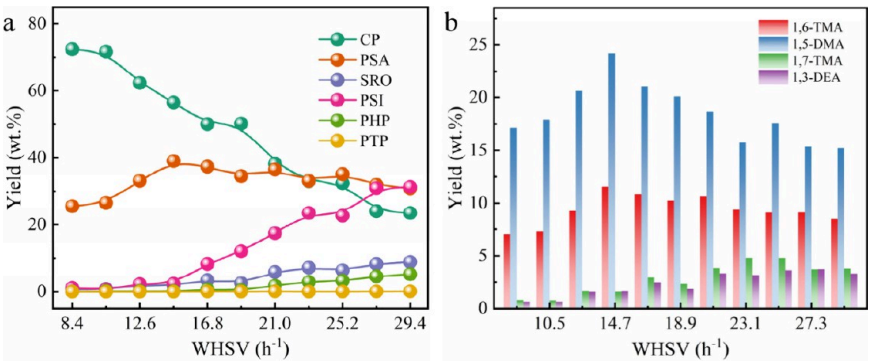

Figure 13. (a) Liquid products and (b) alkyladamantane yields as a function of WHSV at 240 °C under 40 bar of hydrogen pressure over Pt/FAU catalyst.

primary product identified was PTP, and PSI and PSA were not detected on the Pt/FER catalyst. With elevating temperature, the yield of PTP decreased sharply, while that of PHP rose correspondingly. Besides, Pt/MFI showed a similar tendency in product distributions, though the PTP yield was markedly lower than that observed on Pt/FER catalyst under identical conditions. Subsequently, the yield of PSI began to gradually rise. These findings indicated that in the one-step hydroconversion, PHE preferentially underwent hydrosaturation to generate PHP, which was then further converted to form PSI via skeletal isomerization. In addition, only a small amount of PSA and SRO were obtained over the Pt/MFI and Pt/FER catalysts, but considerable yield of CP was gained at higher temperatures, implying that the cracking reaction was emerged due to the further transformation of PSI. The formation of SRO and PSA could be more clearly elucidated using Pt/BEA and Pt/FAU catalysts. As illustrated in Figure 10c-d, the yields of PSA and SRO gradually increased with rising levels of PSI at the temperature range of 190−220 °C. Notably, when the yield of PSI declined, the yield of PSA continued to increase before subsequently declining due to cracking at elevated reaction temperatures. This observation supports the notion that both SRO and PSA could be produced via the conversion of PSI. Furthermore, various cracking products were detected, as depicted in Figure 8. On account of the product distribution analyzed across a series of Pt/zeolite catalysts in Figure 10 and the constituents of CP product, it could be inferred that gaseous alkanes, cyclohexane, alkylcyclohexanes, decalin, and alkyldecalin were formed as a result of the cracking of PSI and SRO. Meanwhile, products such as adamantane and methyladamantane were generated from the cracking of PSA. As a result, the hydroconversion of PHE involved an initial hydrosaturation step to yield PHP, which was subsequently isomerized to yield PSI. This was followed by further transformations leading to the production of SRO and PSA. Ultimately, CP was generated through the cleavage of SRO and PSA. Importantly, the generation of PSA and SRO predominantly occurs within the pores of acidic zeolites.

The experimental results distinctly elucidate that the highly dispersed Pt/FAU sample is the most effective material for the conversion of PAHs into HEAFs. To further evaluate the catalytic properties of Pt/FAU, the reaction was conducted at 240 °C varying the WHSV from 8.4 to 29.4 h^{-1}. Figure 13 depicts the yields of liquid products and PSA as a function of WHSV. The CP yield reduced sharply with the increase in WHSV. Simultaneously, the yield of PSI steadily rose, indicating that the CP was mainly fabricated by the further reaction of PSI. In addition, the yield of PSA showed a slight increase, reaching the maximum of 39.0 wt % at 14.7 h^{-1}. However, as the WHSV continued to improve, the PSA yield declined slightly, while both SRO and PHP demonstrated a noticeable rise. These observations align with the conversion pathways proposed in Scheme 2. In Figure 13b, 1,5-DMA was preponderant under all employed WHSV conditions. As the WHSV improved from 8.4 to 14.7 h^{-1}, the 1,5-DMA yield sustained to heighten, resulting in a volcano-shaped distribution. At 14.7 h^{-1}, the optimal yields of 1,6-TMA, 1,5-DMA, 1,7-TMA, and 1,3-DEA were 11.5 wt %, 24.2, 1.6, and 1.7 wt %, respectively. Moreover, it could be observed that the yields of 1,7-TMA and 1,3-DEA persisted to rise as the WHSV enhanced from 8.4 to 25.2 h^{-1}. This illustrated that the lower yields of 1,7-TMA and 1,3-DEA on Pt/FAU compared to Pt/BEA catalyst were resulted by the further cracking. The highest yields of 1,7-TMA and 1,3-DEA were gained at a WHSV of 25.5 h^{-1}. The most acidic sites, particularly B acid, on the Pt/FAU catalyst likely contributed to the intensified cleavage of PSA product, in line with the evaluation results. Furthermore, Table 4 provides the comparison of the yields and hydroconversion conditions of PSA and SRO from tricyclic hydrocarbons. In this work, the maximum yield of PSA was achieved at 14.7 h^{-1}, in which the optimum yield of HEAFs (42.6 wt %) was obtained at 21.0 h^{-1}, representing the supreme performances reported in the literature. However, the yield of SRO was significantly lower than that of PSA species, indicating that it is more prone to cracking and therefore exhibits greater endothermic capacity.

3.3. Monte Carlo Simulations. The diffusion of intermediates in the porous channels of zeolites markedly impacts the one-step hydroconversion of PAHs. For the sake of gaining deeper insights into the formation pathway of PSA and SRO substances, Monte Carlo simulations were executed to analyze the adsorption and diffusion behavior of PHE and PHP species in the pores. Concurrently, pure silica frameworks were utilized to avoid the effects of polarity. As plotted in Figure S3, supercells were constructed to guarantee similar unit cell dimensions. Specifically, the p (1 × 2 × 2) of MFI, p (2 × 2 × 3) of FER, p (2 × 3 × 1) of BEA, and p (1 × 2 × 1) of FAU were established and optimized to attain their lowest-energy conformations utilizing the COMPASSIII force field, which is frequently applied in zeolite calculations.[68,69] Figure S4 illustrates that the perhydrogenated product PHP displayed a larger three-dimensional size than PHE, leading to a greater diffusion resistance for PHP in the micropores of as-

https://doi.org/10.1021/acs.energyfuels.5c02305
Energy Fuels 2025, 39, 12551−12568

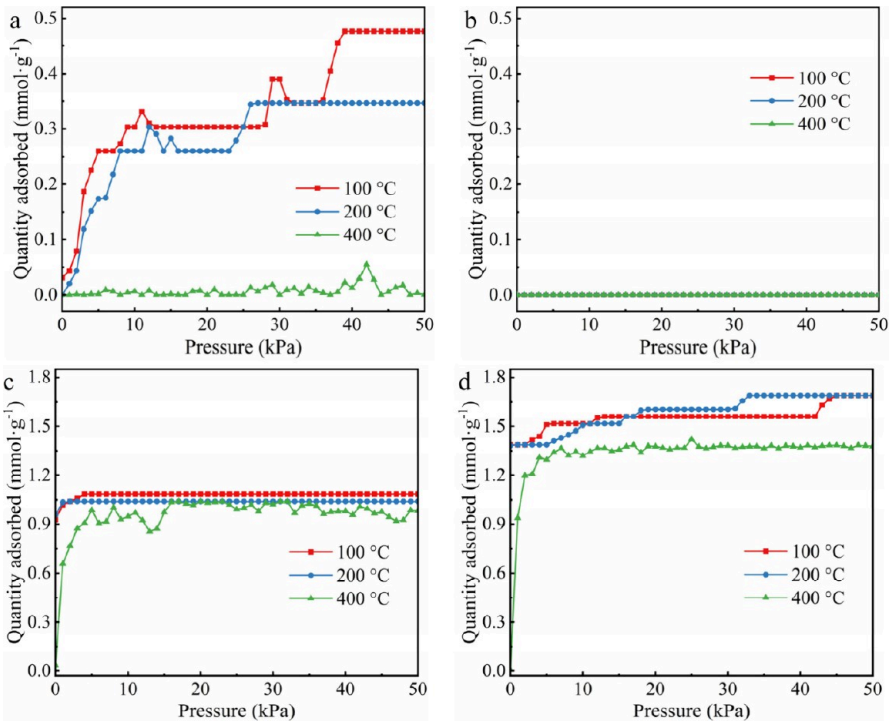

Figure 14. Computational adsorption isotherms of phenanthrene in (a) MFI, (b) FER, (c) BEA, and (d) FAU zeolites at different temperatures.

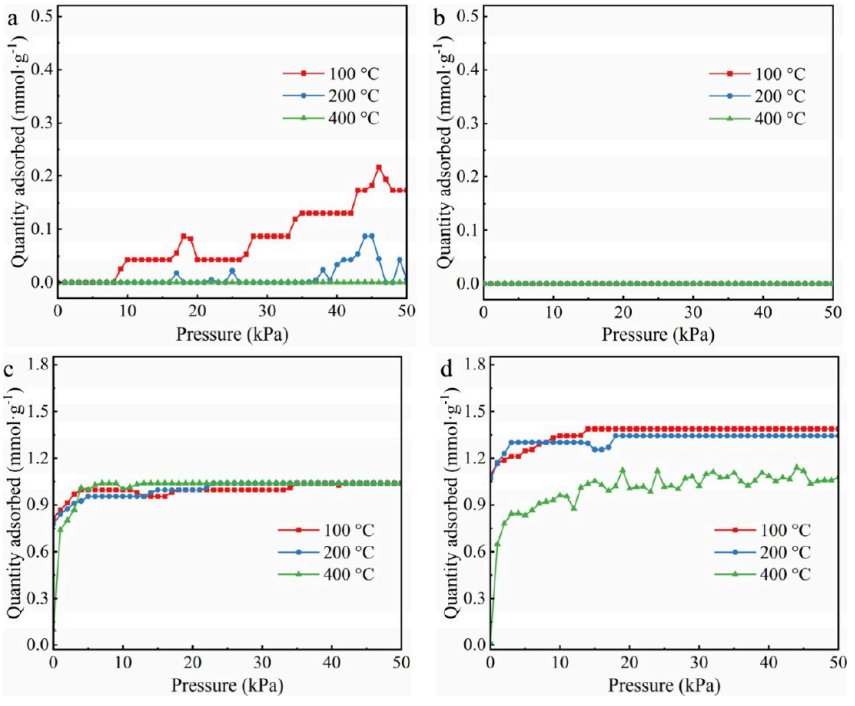

Figure 15. Computational adsorption isotherms of perhydrophenanthrene in (a) MFI, (b) FER, (c) BEA, and (d) FAU zeolites at different temperatures

synthesized Pt/zeolite catalysts. In Figure 14, the adsorption isotherms of PHE in disparate zeolites at 100 °C, 200, and 400 °C are exhibited. It could be investigated that the adsorption capacity declined with increasing temperatures. This trend arose because, at lower temperature, the stronger interaction forces between the adsorbates and the adsorbent could bind the adsorbate molecules more effectively to the adsorbent surface. However, as the temperature increased, the rotation and translation of adsorbates were improved, with higher temperatures supplying the energy needed for desorption. Consequently, PHE molecules more readily desorbed at elevated temperatures, decreasing the adsorption capacity. Besides, the adsorption isotherms for all zeolites adhered to the Langmiur model.[45] With an increase in pressure, the adsorption amounts of PHE initially rise sharply before reaching equilibrium. Figure 14a exhibited that MFI had

https://doi.org/10.1021/acs.energyfuels.5c02305
Energy Fuels 2025, 39, 12551−12568

inferior adsorption ability for PHE, requiring a higher pressure to achieve saturation. At 100 °C, the highest adsorbed quantity of 0.48 mmol·g^{-1} was reached at 39 kPa. When the adsorption temperature was boosted to 400 °C, the adsorbed amount approached zero within the pressure range of 0−50 kPa. Additionally, FER presented a minimal adsorption capacity of zero for PHE under the given conditions (Figure 14b). These phenomena aligned with experimental findings, where Pt/FER demonstrated the poorest catalytic performances for one-step hydroconversion of PHE, while Pt/MFI showed better activities. This suggested that PHE diffusion into pores allowed greater interaction with acidic sites, facilitating hydroconversion.

Furthermore, the BEA zeolite showed much better adsorption characteristics at tested temperatures (Figure 14c). The adsorption capacities only decreased slightly with rising temperature, and it could attain adsorption saturation at relatively low pressure. Even at 400 °C, it maintained a high adsorption capacity of 1.04 mmol·g^{-1} for PHE, which was just 0.04 mmol·g^{-1} lower than the value at 100 °C. In contrast, FAU zeolite (Figure 14d) depicted the highest adsorption capacity for PHE, reaching a saturation capacity of 1.56 mmol·g^{-1} at 100 °C under 39 kPa, 0.48 mmol·g^{-1} higher than that observed for BEA. The reinforced capacity was attributed to the three-dimensional 12-membered ring channel structure and the presence of supercages in FAU. In addition, the greater pore diameters of 0.74 × 0.74 nm facilitated better diffusion of PHE in the pores compared to the other zeolites. Notably, FAU also clarified superior adsorption ability at 400 °C, with a saturated adsorption capacity of 1.42 mmol·g^{-1}. These adsorption trends over MFI, FER, BEA, and FAU zeolites are consistent with the activity data, underscoring the critical role of porous structure in impacting the hydroconversion of PHE, indicating that the hydroconversion of PHE predominantly occurred within the pores of acidic zeolites.

The adsorption of PHP in different zeolites was calculated to further support the conclusion that the high yields of SRO and PSA over Pt/BEA and Pt/FAU catalysts are attributed to their larger pore diameters and more accessible acid sites. Figure 15 exhibits the computational adsorption isotherms of PHP in MFI, FER, BEA, and FAU zeolites. It demonstrated noticeably lower saturation adsorption capacities for PHP compared to PHE. This could be assigned to the larger three-dimensional size of PHP, which increased the diffusion resistance within the micropores. Consequently, PHP required a higher pressure to reach equilibrium at specific temperatures. Interestingly, similar to the adsorption of PHE, temperature had minimal influence on the adsorption amount of PHP (Figure 15c), likely due to the unique framework structure. Lastly, the highest adsorption quantity was observed in FAU (Figure 15d), with an optimal adsorption of 1.39 mmol·g^{-1} achieved at 100 °C under a pressure of 14 kPa. Much better adsorption capacities of PHP were obtained on BEA and FAU zeolites. Therefore, Pt/BEA and Pt/FAU catalysts gave excellent yields for PSA and SRO species.

The adsorption configurations of PHE and PHP in various zeolites were calculated at 200 °C with a fixed pressure of 30 kPa. Figures 16 and 17 display the optimized lowest-energy conformations of PHE and PHP in different zeolites, respectively. Obviously, no adsorbed PHE or PHE molecules were discovered in the supercell of the FER zeolite. In MFI zeolite, only two PHE molecules were observed in the straight channels (Figure 16a), while PHP was not detected (Figure 17a). Conversely, BEA and FAU zeolites exhibited a significant number of adsorbed PHE and PHP molecules, in which FAU showed a greater number of adsorbed molecules due to its larger pore sizes and existence of supercages. A substantial amount of PHE and PHP was located in the pores and supercages of FAU (Figures 16d and 17d). This observation aligns with the results obtained from the adsorption isotherms, further supporting the conclusion that PSA and SRO are formed within the pores and supercages of the FAU zeolite.

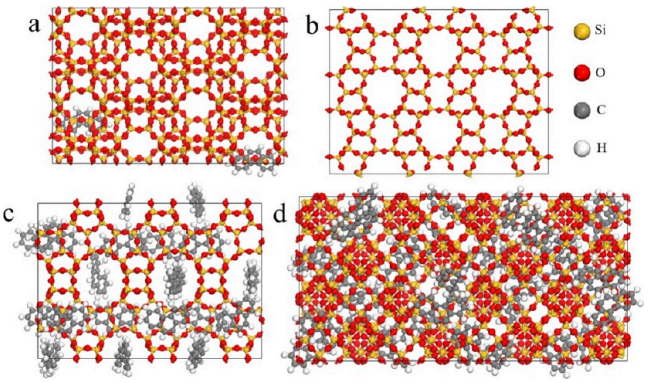

Figure 16. Optimized lowest-energy conformation of phenanthrene adsorbed in (a) MFI, (b) FER, (c) BEA, and (d) FAU zeolites.

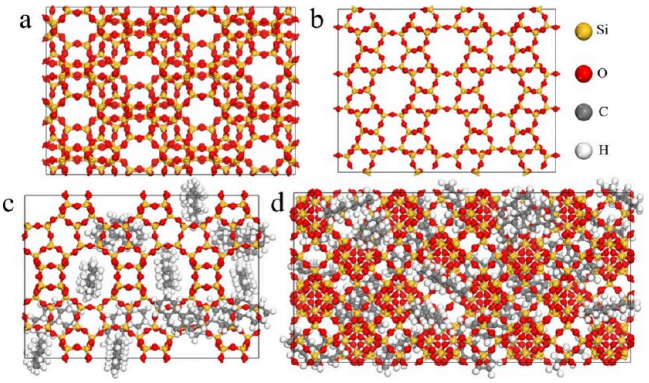

Figure 17. Optimized lowest-energy conformation of perhydrophenanthrene adsorbed in (a) MFI, (b) FER, (c) BEA, and (d) FAU zeolites.

3.4. The Properties of Synthesized High-Density Endothermic Aviation Fuels. The density, volumetric net heat of combustion (VHOC), and ignition delay time (ID) of prepared HEAFs was measured to elucidate its superior fuel properties. Meanwhile, the results were compared against the widely used U.S. military high-density fuel JP-10.[70] This comparison helps to highlight the advantages of the synthesized HEAFs in terms of the energy content and combustion characteristics, which are critical factors for their potential applications. As compiled in Table 5, the fuels synthesized in this work exhibited higher density of 0.957 g/

Table 5. Fuel Properties of As-Synthesized HEAFs and JP-10 Samples

Fuels	Density (20 °C, g/mL)	VHOC (MJ/L)[a]	ID (ms)[b]
This work	0.957	40.3	2935
JP-10	0.936	39.4	2412

[a]Volumetric net heat of combustion. [b]Ignition delay time.

https://doi.org/10.1021/acs.energyfuels.5c02305
Energy Fuels 2025, 39, 12551−12568

mL and VHOC of 40.3 MJ/L, which can significantly promote the flight performance of aircraft. Furthermore, according to the combustion flame images plotted in Figure 18, HEAFs demonstrated a longer ID of 2935 ms compared to JP-10, suggesting better thermal oxidation stability.

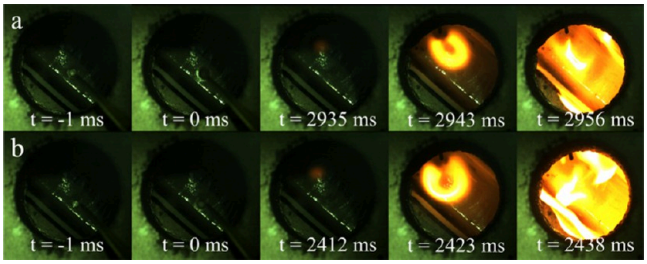

Figure 18. Photographs of fuel combustion flame images of as-synthesized (a) HEAFs and (b) JP-10 samples.

4. CONCLUSIONS

In conclusion, MFI, FER, BEA, and FAU zeolites with diverse topological frameworks supported by highly dispersed Pt catalysts were employed to investigate the hydroconversion pathways of PHE to PSA and SRO species for HEAFs in a fixed-bed microreactor. The conversion network was elucidated as follows: PHE was preferentially hydrosaturated to PHP and then isomerized into PSI, followed by rearrangement to form PSA and SRO products, and finally CP was yielded by cracking. Among the catalysts, Pt/BEA and Pt/FAU catalysts showed superior isomerization and ring-opening activities due to their larger pore sizes and accessible acid sites. Meanwhile, the optimum HEAFs yield of 42.6 wt %, which is the optimal performance reported in literature to our knowledge, was accomplished at 240 °C and WHSV of 21.0 h^{-1} on Pt/FAU. Moreover, Pt/MFI and Pt/FER catalysts showed inferior isomerization and selective ring-opening activities, but Pt/MFI had superior deep hydrosaturation properties because of its more accessible acid sites. PSA and SRO were formed in the microporous channels of zeolite rather than on the external surface, with 1,5-DMA, 1,3-DEA, 1,7-TMA, and 1,6-TMA as the primary components in PSA product. The generation of PSA requires complex reactions, including dehydrogenation, protonation, rearrangement, and alkylation. Theoretical simulations further verified the improved catalytic activities of the Pt/BEA and Pt/FAU catalysts. FAU exhibited optimal adsorption because of its three-dimensional 12-membered ring channels and supercages, confirming that the generation of PSA and SRO predominantly occurred within the pores of zeolites by the cycloisomerization of PSI. Furthermore, the as-synthesized HEAFs illustrated fuel properties superior to those of JP-10, highlighting excellent potential as advanced aviation fuel.

■ ASSOCIATED CONTENT

Supporting Information

The Supporting Information is available free of charge at https://pubs.acs.org/doi/10.1021/acs.energyfuels.5c02305.

Schematic illustration of hot-plate ignition equipment, comprehensive GC × GC-FID chromatogram of PHP stereoisomers, optimized structural models of different zeolites, and optimized structural models and dimensions of phenanthrene and perhydrophenanthrene molecules (PDF)

■ AUTHOR INFORMATION

Corresponding Author

Qingfa Wang − *Key Laboratory for Green Chemical Technology of Ministry of Education, School of Chemical Engineering and Technology, Tianjin University, Tianjin 300072, P. R. China; Collaborative Innovation Center of Chemical Science and Engineering (Tianjin), Tianjin University, Tianjin 300072, P. R. China;* orcid.org/0000-0002-0665-7586; Phone: +86-22-27892340; Email: qfwang@tju.edu.cn

Authors

Xiaopo Niu − *Institute of Catalytic Reaction Engineering, College of Chemical Engineering, Zhejiang University of Technology, Hangzhou 310014, P. R. China; Key Laboratory for Green Chemical Technology of Ministry of Education, School of Chemical Engineering and Technology, Tianjin University, Tianjin 300072, P. R. China; Collaborative Innovation Center of Chemical Science and Engineering (Tianjin), Tianjin University, Tianjin 300072, P. R. China*

Feipeng Huang − *Institute of Catalytic Reaction Engineering, College of Chemical Engineering, Zhejiang University of Technology, Hangzhou 310014, P. R. China; College of Chemical and Biological Engineering, Zhejiang University, Hangzhou 310058, P. R. China*

Wenli Zhao − *Key Laboratory for Green Chemical Technology of Ministry of Education, School of Chemical Engineering and Technology, Tianjin University, Tianjin 300072, P. R. China; Collaborative Innovation Center of Chemical Science and Engineering (Tianjin), Tianjin University, Tianjin 300072, P. R. China*

Danni Liu − *Key Laboratory for Green Chemical Technology of Ministry of Education, School of Chemical Engineering and Technology, Tianjin University, Tianjin 300072, P. R. China; Collaborative Innovation Center of Chemical Science and Engineering (Tianjin), Tianjin University, Tianjin 300072, P. R. China*

Yue Qin − *Key Laboratory for Green Chemical Technology of Ministry of Education, School of Chemical Engineering and Technology, Tianjin University, Tianjin 300072, P. R. China; Collaborative Innovation Center of Chemical Science and Engineering (Tianjin), Tianjin University, Tianjin 300072, P. R. China*

Xiangwen Zhang − *Key Laboratory for Green Chemical Technology of Ministry of Education, School of Chemical Engineering and Technology, Tianjin University, Tianjin 300072, P. R. China; Collaborative Innovation Center of Chemical Science and Engineering (Tianjin), Tianjin University, Tianjin 300072, P. R. China*

Hanfeng Lu − *Institute of Catalytic Reaction Engineering, College of Chemical Engineering, Zhejiang University of Technology, Hangzhou 310014, P. R. China;* orcid.org/0000-0001-8934-8270

Quanli Ke − *Institute of Catalytic Reaction Engineering, College of Chemical Engineering, Zhejiang University of Technology, Hangzhou 310014, P. R. China;* orcid.org/0000-0002-9123-5803

Complete contact information is available at: https://pubs.acs.org/10.1021/acs.energyfuels.5c02305

https://doi.org/10.1021/acs.energyfuels.5c02305
Energy Fuels 2025, 39, 12551−12568

Author Contributions

Xiaopo Niu: Methodology, Validation, Formal analysis, Data curation, Investigation, Writing-Original Draft. **Feipeng Huang**: Formal analysis, Validation, Investigation. **Wenli Zhao**: Formal analysis, Validation, Investigation. **Danni Liu**: Formal analysis, Investigation. **Yue Qin**: Investigation, Data curation. **Xiangwen Zhang**: Investigation, Project administration, Resources. **Hanfeng Lu**: Formal analysis. **Quanli Ke**: Investigation. **Qingfa Wang**: Resources, Project administration, Funding acquisition, Writing-Review & Editing, Supervision.

Notes

The authors declare no competing financial interest.

■ ACKNOWLEDGMENTS

The financial supports from the National Natural Science Foundation of China (Grant No. 22279088) and the China Postdoctoral Science Foundation (Grant No. 2024M752867) are gratefully acknowledged. The authors also thank the team at Shiyanjia Lab (www.shiyanjia.com) for assistance with material characterization.

■ REFERENCES

(1) Wang, W.; Pu, B.; Ma, C.; Shi, C.; Pan, L.; Zhang, X.; Zou, J.-J. Pd/C catalytic cyclopropanation of polycyclic olefins for synthesis of high-energy-density strained fuels. *AlChE J.* **2023**, *69* (7), No. e18085.

(2) Zou, J.-J.; Zhang, X.; Pan, L. *High-Energy-Density Fuels for Advanced Propulsion: Design and Synthesis*; John Wiley & Sons, 2020.

(3) Xie, J.; Zhang, J.; Wang, X.; Xie, J.; Yang, B.; Liang, Y.; Zou, J.-J.; Zhang, Q. Synthesis of JP-10 analogues high-density fuels via one-pot Diels-Alder/hydrodeoxygenation reaction. *Fuel* **2024**, *361*, 130738.

(4) Zhang, X.; Song, M.; Liu, J.; Zhang, Q.; Chen, L.; Ma, L. Synthesis of high density and low freezing point jet fuels range cycloalkanes with cyclopentanone and lignin-derived vanillins. *J. Energy Chem.* **2023**, *79*, 22−30.

(5) Liu, Q.; Pan, L.; Jia, T.; Zhang, X.; Zou, J.-J. Alkyl-adamantane as high-density endothermic fuel: Synthesis and thermal cracking performance. *Fuel* **2022**, *324*, 124688.

(6) Hubesch, R.; Mazur, M.; Selvakannan, P. R.; Föger, K.; Lee, A. F.; Wilson, K.; Bhargava, S. Endothermic catalytic cracking of liquid hydrocarbons for thermal management of high-speed flight vehicles. *Sustainable Energy Fuels* **2022**, *6* (7), 1664−1686.

(7) Abrantes, I.; Ferreira, A. F.; Silva, A.; Costa, M. Sustainable aviation fuels and imminent technologies - CO_2 emissions evolution towards 2050. *Journal of Cleaner Production* **2021**, *313*, 127937.

(8) Bergero, C.; Gosnell, G.; Gielen, D.; Kang, S.; Bazilian, M.; Davis, S. J. Pathways to net-zero emissions from aviation. *Nature Sustainability* **2023**, *6* (4), 404−414.

(9) Wu, L.; Xin, J.; Wang, Y.; Zhang, K.; Zhang, J.; Sun, J.; Zou, R.; Liang, J. Hollow ZSM-5 encapsulated with single Ga-atoms for the catalytic fast pyrolysis of biomass waste. *Journal of Energy Chemistry* **2023**, *84*, 363−373.

(10) Wei, X.-Y.; Bai, X.; Ma, F.-Y.; Zong, Z.-M.; Zhao, W.; Ni, Z.-H.; Fan, X.; Sun, L.-B.; Cao, J.-P.; Zhao, Y.-P.; et al. Advances in Catalytic Hydroconversion of Typical Heavy Carbon Resources under Mild Conditions. *Energy Fuels* **2023**, *37* (17), 12570−12588.

(11) Leite, L.; Benazzi, E.; Marchal-George, N. Hydrocracking of phenanthrene over bifunctional Pt catalysts. *Catal. Today* **2001**, *65* (2), 241−247.

(12) Jing, J.; Guo, Z.; Li, Z.; Chen, Y.; Li, H.; Li, W.-Y. Enhancing phenanthrene hydrogenation via controllable phosphate deposition over Ni_2P/Al_2O_3 catalysts. *Chem. Eng. Sci.* **2023**, *282*, 119251.

(13) Zhao, J.; Wang, X.; Niu, H.; Liu, J.; Liang, C.; Li, C. Hydroisomerization Principles of Acenaphthene to Alkyladamantanes over Modified USY-Supported Pt Catalysts. *Energy Fuels* **2024**, *38* (8), 7181−7195.

(14) Jampaiah, D.; Murzin, D. Y.; Lee, A. F.; Schaller, D.; Bhargava, S. K.; Tabulo, B.; Wilson, K. Catalytic selective ring opening of polyaromatics for cleaner transportation fuels. *Energy Environ. Sci.* **2022**, *15* (5), 1760−1804.

(15) Petrukhina, N. N.; Vinnikova, M. A.; Maksimov, A. L. Production of High-Density Jet and Diesel Fuels by Hydrogenation of Highly Aromatic Fractions. *Russ. J. Appl. Chem.* **2018**, *91* (8), 1223−1254.

(16) Xie, J.; Zhang, H.; Jia, T.; Xie, J.; Zou, J.-J. Synthesis and fuel properties of high-density and low-freezing-point asymmetric cycloalkyl adamantane. *Fuel Process. Technol.* **2023**, *244*, 107707.

(17) Niu, X.; Sun, J.; Zhao, W.; Yang, X.; Zhang, X.; Wang, Q. Strong electronic metal-support interactions on supported Pt catalysts for efficient perhydrogenation of polyaromatics to aviation fuels. *Fuel Process. Technol.* **2023**, *241*, 107622.

(18) Zhao, W.; Yu, H.; Peng, S.; Liu, W.; Zhang, W.; Mei, D. Mechanistic Understanding of Anthracene Hydrocracking over HY Zeolite Encapsulated Single-Atom Pt Catalysts. *ACS Catal.* **2024**, *14* (11), 8836−8855.

(19) Qi, L.; Peng, C.; Cheng, Z.; Zhou, Z. Selective hydrocracking of poly-aromatics to mono-aromatics in a catalyst grading system of $NiMo/Al_2O_3$-HY and NiMo/Beta. *Fuel* **2023**, *351*, 128941.

(20) Wang, D.; Li, J.; Ma, H.; Yang, C.; Pan, Z.; Qu, W.; Tian, Z. Layer-structure adjustable MoS_2 catalysts for the slurry-phase hydrogenation of polycyclic aromatic hydrocarbons. *J. Energy Chem.* **2021**, *63*, 294−304.

(21) Korre, S. C.; Klein, M. T.; Quann, R. J. Polynuclear Aromatic Hydrocarbons Hydrogenation. 1. Experimental Reaction Pathways and Kinetics. *Ind. Eng. Chem. Res.* **1995**, *34* (1), 101−117.

(22) Yang, C.; Wang, D.; Huang, R.; Han, J.; Ta, N.; Ma, H.; Qu, W.; Pan, Z.; Wang, C.; Tian, Z. Highly active and stable MoS_2-TiO_2 nanocomposite catalyst for slurry-phase phenanthrene hydrogenation. *Chin. J. Catal.* **2023**, *46*, 125−136.

(23) Tang, T.; Yin, C.; Wang, L.; Ji, Y.; Xiao, F. Good sulfur tolerance of a mesoporous Beta zeolite-supported palladium catalyst in the deep hydrogenation of aromatics. *J. Catal.* **2008**, *257* (1), 125−133.

(24) Cuauhtémoc-López, I.; Jiménez-Vázquez, A.; Estudillo-Wong, L. A.; Torres-Torres, G.; Pérez-Vidal, H.; Barrera-Salgado, M.; López-González, R.; De la Cruz-Romero, D. Naphthalene hydrogenation using Rh/Fe_2O_3-TiO_2 magnetic catalysts. *Catal. Today* **2021**, *360*, 176−184.

(25) Liu, Z.; Wang, E.; Mei, J.; Wang, A.; Zou, Y.; Wang, C.; Shang, H.; Gong, Y.; Duan, A.; Xu, C.; et al. Hierarchical porous Pt/Hβ catalyst with controllable acidity for efficient hydrogenation of naphthalene. *Chemical Engineering Journal* **2024**, *481*, 148763.

(26) Jing, J.-Y.; Wang, J.-Z.; Liu, D.-C.; Qie, Z.-Q.; Bai, H.-C.; Li, W.-Y. Naphthalene Hydrogenation Saturation over Ni_2P/Al_2O_3 Catalysts Synthesized by Thermal Decomposition of Hypophosphite. *ACS Omega* **2020**, *5* (48), 31423−31431.

(27) Furimsky, E. Metal carbides and nitrides as potential catalysts for hydroprocessing. *Appl. Catal., A* **2003**, *240* (1), 1−28.

(28) Shan, J.; Wang, H.; Yoo, P.; Nguyen, L.; Chiang, F.-K.; Lee, S.; Liao, P.; Cheng, J. Facile Synthesis of Pt Carbide Nanomaterials and Their Catalytic Applications. *ACS Materials Letters* **2021**, *3* (2), 179−186.

(29) Yu, Y.; Guan, Y.; Zhang, P.; Liu, X.; Zhao, Y.; Zhuang, J.; Zhao, Q.; Wang, Y.; Qian, Y.; Zhu, X.; et al. Identifying the Location of Real Active Sites in ZSM-5 Zeolites for Tetralin Conversion into Light Aromatics. *Energy Fuels* **2023**, *37* (4), 3011−3022.

(30) Qi, J.; Guo, Y.; Jia, H.; Fan, B.; Gao, H.; Qin, B.; Ma, J.; Du, Y.; Li, R. Unpredictable properties of industrial HY zeolite for tetralin hydrocracking. *Fuel Process. Technol.* **2023**, *240*, 107586.

(31) Askarli, S.; Mukhambetov, I.; Chung, S.-H.; Awwad, M.; Almeida, J. N.; Komaty, S.; Navarro de Miguel, J. C.; Li, T.; Ruiz-Martínez, J. Influence of Extra-Framework Aluminum Species on the Catalytic Properties of Acidic USY Zeolite in (Hydro)cracking Reactions. *ACS Catal.* **2024**, *14*, 13630−13639.

https://doi.org/10.1021/acs.energyfuels.5c02305
Energy Fuels 2025, 39, 12551−12568

(32) Brito, L.; Pirngruber, G. D.; Guillon, E.; Albrieux, F.; Martens, J. A. Hydroconversion of Perhydrophenanthrene over Bifunctional Pt/H-USY Zeolite Catalyst. *ChemCatChem.* **2020**, *12* (13), 3477−3488.
(33) Brito, L.; Pirngruber, G. D.; Perez-Pellitero, J.; Guillon, E.; Albrieux, F.; Martens, J. A. Shape selectivity effects in the hydroconversion of perhydrophenanthrene over bifunctional catalysts. *Catal. Sci. Technol.* **2021**, *11* (23), 7667−7682.
(34) Wang, L.; Chen, Y.; Jin, S.; Chen, X.; Liang, C. Selective Ring-Shift Isomerization in Hydroconversion of Fluorene over Supported Platinum Catalysts. *Energy Fuels* **2016**, *30* (4), 3403−3412.
(35) Li, K.; Cui, T.; Zhao, J.; Liang, C.; Li, C. Regulate the mesopores and acidic structure of Pt/USY zeolite catalyst for improved performance in the hydroisomerization of phenanthrene to alkyl-adamantane. *Chem. Eng. Sci.* **2023**, *279*, 118957.
(36) Wang, X.; Li, X.; Li, W. Effect of support acidity on hydrogenation of phenanthrene to alkyl adamantane over Pt/USY catalysts. *CIESC Journal* **2021**, *72* (10), 5196−5205.
(37) Munnik, P.; de Jongh, P. E.; de Jong, K. P. Recent developments in the synthesis of supported catalysts. *Chem. Rev.* **2015**, *115* (14), 6687−6718.
(38) Niu, X.; Zhao, R.; Han, Y.; Zhang, X.; Wang, Q. Highly dispersed platinum clusters anchored on hollow ZSM-5 zeolite for deep hydrogenation of polycyclic aromatic hydrocarbons. *Fuel* **2022**, *326*, 125021.
(39) Mehrabadi, B. A. T.; Eskandari, S.; Khan, U.; White, R. D.; Regalbuto, J. R. A Review of Preparation Methods for Supported Metal Catalysts. *Adv. Catal.* **2017**, *61*, 1−35.
(40) Eskandari, S.; Tate, G.; Leaphart, N. R.; Regalbuto, J. R. Nanoparticle Synthesis via Electrostatic Adsorption Using Incipient Wetness Impregnation. *ACS Catal.* **2018**, *8* (11), 10383−10391.
(41) Emeis, C. Determination of Integrated Molar Extinction Coefficients for Infrared Absorption Bands of Pyridine Adsorbed on Solid Acid Catalysts. *J. Catal.* **1993**, *141* (2), 347−354.
(42) Xu, Y.; Yuan, X.; Chen, M.; Dong, A.; Liu, B.; Jiang, F.; Yang, S.; Liu, X. Identification of atomically dispersed Fe-oxo species as new active sites in HZSM-5 for efficient non-oxidative methane dehydroaromatization. *J. Catal.* **2021**, *396*, 224−241.
(43) Zhang, M.; Chen, Y.; Wang, L.; Zhang, Q.; Tsang, C.-W.; Liang, C. Shape Selectivity in Hydroisomerization of Hexadecane over Pt Supported on 10-Ring Zeolites: ZSM-22, ZSM-23, ZSM-35, and ZSM-48. *Ind. Eng. Chem. Res.* **2016**, *55* (21), 6069−6078.
(44) Qi, L.; Zhang, Y.; Conrad, M. A.; Russell, C.; Miller, J. T.; Bell, A. T. Ethanol Conversion to Butadiene over Isolated Zinc and Yttrium Sites Grafted onto Dealuminated Beta Zeolite. *J. Am. Chem. Soc.* **2020**, *142* (34), 14674−14687.
(45) Thommes, M.; Kaneko, K.; Neimark, A. V.; Olivier, J. P.; Rodriguez-Reinoso, F.; Rouquerol, J.; Sing, K. S. W. Physisorption of gases, with special reference to the evaluation of surface area and pore size distribution (IUPAC Technical Report). *Pure Appl. Chem.* **2015**, *87* (9−10), 1051−1069.
(46) Tao, H.; Yang, H.; Liu, X.; Ren, J.; Wang, Y.; Lu, G. Highly stable hierarchical ZSM-5 zeolite with intra- and inter-crystalline porous structures. *Chem. Eng. J.* **2013**, *225*, 686−694.
(47) Mintova, S.; Jaber, M.; Valtchev, V. Nanosized microporous crystals: emerging applications. *Chem. Soc. Rev.* **2015**, *44* (20), 7207−7233.
(48) Treps, L.; Gomez, A.; de Bruin, T.; Chizallet, C. Environment, Stability and Acidity of External Surface Sites of Silicalite-1 and ZSM-5 Micro and Nano Slabs, Sheets, and Crystals. *ACS Catal.* **2020**, *10* (5), 3297−3312.
(49) Cheng, K.; van der Wal, L. I.; Yoshida, H.; Oenema, J.; Harmel, J.; Zhang, Z.; Sunley, G.; Zečević, J.; de Jong, K. P. Impact of the Spatial Organization of Bifunctional Metal-Zeolite Catalysts on the Hydroisomerization of Light Alkanes. *Angew. Chem., Int. Ed.* **2020**, *59* (9), 3592−3600.
(50) Qin, Z.; Wang, B.; Asano, N.; Wang, L.; Zhou, Y.; Liu, X.; Shen, B.; Mintova, S.; Asahina, S.; Valtchev, V. Towards a comprehensive understanding of mesoporosity in zeolite Y at the single particle level. *Inorganic Chemistry Frontiers* **2022**, *9*, 2365−2373.
(51) Niu, X.; Feng, F.; Yuan, G.; Zhang, X.; Wang, Q. Hollow MFI Zeolite Supported Pt Catalysts for Highly Selective and Stable Hydrodeoxygenation of Guaiacol to Cycloalkanes. *Nanomaterials* **2019**, *9* (3), 362.
(52) Luo, M.; Wang, Q.; Li, G.; Zhang, X.; Wang, L.; Han, L. $AlCl_3$-promoted MCM-41-supported platinum catalysts with high activity and sulfur-tolerance for tetralin hydrogenation: Effect of Pt-Al interaction. *Catal. Commun.* **2013**, *35*, 6−10.
(53) Luo, M.; Wang, Q.; Zhang, X.; Wang, L.; Hu, B. $Al(CH_3)_3$-promoted Pt/MCM-41 catalysts for tetralin hydrogenation in the presence of benzothiophene and promotion mechanism of Al-promoted Pt/MCM-41 catalysts. *RSC Adv.* **2015**, *5* (53), 42468−42476.
(54) Kim, S.; Park, G.; Woo, M. H.; Kwak, G.; Kim, S. K. Control of Hierarchical Structure and Framework-Al Distribution of ZSM-5 via Adjusting Crystallization Temperature and Their Effects on Methanol Conversion. *ACS Catal.* **2019**, *9* (4), 2880−2892.
(55) Ro, I.; Qi, J.; Lee, S.; Xu, M.; Yan, X.; Xie, Z.; Zakem, G.; Morales, A.; Chen, J. G.; Pan, X.; et al. Bifunctional hydroformylation on heterogeneous Rh-WO_x pair site catalysts. *Nature* **2022**, *609* (7926), 287−292.
(56) Berenguer, A.; Bennett, J. A.; Hunns, J.; Moreno, I.; Coronado, J. M.; Lee, A. F.; Pizarro, P.; Wilson, K.; Serrano, D. P. Catalytic hydrodeoxygenation of m-cresol over Ni_2P/hierarchical ZSM-5. *Catal. Today* **2018**, *304*, 72−79.
(57) Shi, X.; Wang, Q.; Violi, A. Reaction pathways for the formation of five-membered rings onto polyaromatic hydrocarbon framework. *Fuel* **2021**, *283*, 119023.
(58) Wang, H.; Frenklach, M. Transport properties of polycyclic aromatic hydrocarbons for flame modeling. *Combust. Flame* **1994**, *96* (1), 163−170.
(59) Sinfelt, J.; Lucchesi, P. Kinetic Evidence for the Migration of Reactive Intermediates in Surface Catalysis. *J. Am. Chem. Soc.* **1963**, *85* (21), 3365−3367.
(60) Qin, X.; Yu, W.; Ye, L.; Shen, H.; Liu, J.; Murad, A.; Xie, J.; Hou, L.; Pu, X.; Han, X.; et al. Reaction laws of polycyclic aromatic hydrocarbons and heteroatomic compounds in hydrocracking process. *Fuel* **2023**, *332*, 126242.
(61) Xie, J.; Shi, C.; Zhao, Y.; Pan, L.; Zhang, X.; Zou, J.-J. Synthesis and comprehensive fuel properties of mono-substituted alkyl adamantanes for advanced aerospace propulsion. *Fuel Process. Technol.* **2021**, *218*, 106842.
(62) Fang, T.; Xie, Y.; Li, L.; He, Y.; Yang, X.; Zhang, L.; Jia, W.; Huang, H.; Li, J.; Zhu, Z. High-efficiency hydrocracking of phenanthrene into BTX aromatics over a Ni-modified lamellar-crystal HY zeolite. *Phys. Chem. Chem. Phys.* **2022**, *24* (15), 8624−8630.
(63) Shamzhy, M.; Opanasenko, M.; Concepcion, P.; Martinez, A. New trends in tailoring active sites in zeolite-based catalysts. *Chem. Soc. Rev.* **2019**, *48* (4), 1095−1149.
(64) Dusselier, M.; Davis, M. E. Small-Pore Zeolites: Synthesis and Catalysis. *Chem. Rev.* **2018**, *118* (11), 5265−5329.
(65) Saginayev, A. Syntheses, Geometrical and Electronic Structure of Alkyladamantanes and Their Thermodynamic Characteristic According to the Density Functional Theory. *Science Journal of Chemistry* **2018**, *6* (4), 50−55.
(66) Schneider, A.; Warren, R. W.; Janoski, E. J. Formation of Perhydrophenalenes and Polyalkyladamantanes by Isomerization of Tricyclic Perhydroaromatics. *J. Org. Chem.* **1966**, *31* (5), 1617−1625.
(67) Rollmann, L. D.; Green, L. A.; Bradway, R. A.; Timken, H. K. C. Adamantanes from petroleum with zeolites. *Catal. Today* **1996**, *31* (1), 163−169.
(68) Arı, M. U.; Ahunbay, M. G.; Yurtsever, M.; Erdem-Şenatalar, A. Molecular Dynamics Simulation of Water Diffusion in MFI-Type Zeolites. *J. Phys. Chem. B* **2009**, *113* (23), 8073−8079.
(69) Sun, Y.; Hou, T.; Sun, S.; Du, H.; Fu, S.; Wang, J. Synergistic effects of zeolite and oxygen vacancies in SnO_2 for formaldehyde

sensing: Molecular simulation insights & experimental verification. *Appl. Surf. Sci.* **2022**, *604*, 154511.
(70) Liu, Y.; Ma, C.; Shi, C.; Pan, L.; Xie, J.; Gong, S.; Zhang, Y.-C.; Nie, G.; Zhang, X.; Zou, J.-J. Synthesis of strained high-energy rocket bio-kerosene via cyclopropanation of myrcene. *Fuel Process. Technol.* **2020**, *201*, 106339.

https://doi.org/10.1021/acs.energyfuels.5c02305
Energy Fuels 2025, 39, 12551−12568